# A numerical investigation of the mechanics of intracranial aneurysms walls: Assessing the influence of tissue hyperelastic laws and heterogeneous properties on the stress and stretch fields

I. L. Oliveira[d,*], P. Cardiff[b], C.E. Baccin[c], J.L. Gasche[a]

[a] *São Paulo State University (UNESP), School of Engineering, Mechanical Engineering Department*
[b] *University College Dublin (UCD), School of Mechanical and Materials Engineering, Dublin, Ireland*
[c] *Interventional Neuroradiology/Endovascular Neurosurgery, Beth Israel Deaconess Medical Center, Harvard Medical School, Boston, MA, US*
[d] *São Paulo State University (UNESP), School of Engineering, Mechanical Engineering Department, Thermal Sciences Building, Avenida Brasil, 56, Ilha Solteira - SP, Brazil*

---

**Abstract**

Numerical simulations have been extensively used in the past two decades for the study of intracranial aneurysms (IAs), a dangerous disease that occurs in the arteries that reach the brain. They may affect up to 10 % of the world's population, with up to 50 % mortality rate, in case of rupture. Physically, the blood flow inside IAs should be modeled as a fluid-solid interaction problem. However, the large majority of those works have focused on the hemodynamics of the intra-aneurysmal flow, while ignoring the wall tissue's mechanical response entirely, through rigid-wall modeling, or using limited modeling assumptions for the tissue mechanics. One of the explanations is the scarce data on the properties of IAs walls, thus limiting the use of better modeling options. Unfortunately, this situation is still the case, thus our present study investigates the effect of different modeling approaches to simulate the motion of an IA. We used three hyperelastic laws — the Yeoh law, the three-parameter Mooney-Rivlin law, and a Fung-like law with a single parameter — and two different ways of modeling the wall thickness and tissue mechanical properties — one assumed that both were uniform while the other accounted for the heterogeneity of the wall by using a "hemodynamics-driven" approach in which both thickness and material constants varied spatially with the cardiac-cycle-averaged hemodynamics. Pulsatile numerical simulations, with patient-specific vascular geometries harboring IAs, were carried out using the one-way fluid-solid interaction solution strategy implemented in solids4foam, an extension of OpenFOAM®, in which the blood flow is solved and applied as the driving force of the wall motion. We found that different wall morphology models yield smaller absolute differences in the mechanical response than different hyperelastic laws. Furthermore, the stretch levels of IAs walls were more sensitive to the hyperelastic and material constants than the stress. These findings could be used to guide modeling

decisions on IA simulations, since the computational behavior of each law was different, for example, with the Yeoh law yielding the smallest computational time.

*Keywords:* intracranial aneurysms, hyperelasticity, wall morphology, mechanical response, numerical simulations

---

**Non-standard Acronyms**

**1WFSI** One-way Fluid-solid Interaction
**BC** Boundary Condition
**DSA** Digital Subtraction Angiography
**IA** Intracranial Aneurysm
**ICA** Internal Carotid Artery
**MCA** Middle Cerebral Artery
**MR** Mooney-Rivlin
**OSI** Oscillatory Shear Index
**TAWSS** Time-averaged Wall Shear Stress
**WLR** Wall-to-lumen Ratio

**Latin Symbols**

$A$ Area of a surface or region
$E$ Young's modulus of a solid
$J$ Jacobian (determinant of the deformation gradient)
$S$ Generic representation of surface (or patch of another surface)
$T$ Cardiac period
$V$ Volume of a region in spatial coordinates
$\bar{q}_a$ Mean blood flow rate through an artery's section
$\sigma_1$ Largest principal eigenvalue of the Cauchy stress tensor
$p_o$ Intracranial pressure
$\lambda_1$ Largest eigenvalue of the stretch tensor
$\mathcal{M}$ Generic representation of a metric of the stress or stretch fields over the wall of an aneurysm
$\mathcal{R}$ The group of ruptured aneurysms
$\mathcal{U}$ The group of unruptured aneurysms
$WLR$ Wall-to-lumen ratio
$\boldsymbol{C}$ Right Green-Cauchy deformation tensor
$\boldsymbol{F}$ Deformation gradient tensor
$\boldsymbol{I}$ Second-order identity tensor
$\boldsymbol{S}$ Second Piola-Kirchhoff stress tensor
$\boldsymbol{n}$ Unit normal vector to the surface $S$ pointing outwards
$\boldsymbol{t}$ Traction vector
$\boldsymbol{u}$ Solid displacement vector
$\boldsymbol{v}$ Material velocity
$\boldsymbol{x}$ Eulerian or spatial coordinates system (Cartesian coordinates)
$d_a$ Diameter of an aneurysm's parent artery section
$d_l$ Vasculature lumen diameter at a specified section
$e_{ia}$ Thickness field of an aneurysm's wall
$f_a$ Scale factor used on the calculation of the aneurysm thickness
$g_n$ Geodesic distance of the vasculature to the aneurysm neck line
$p$ Pressure field
$t$ Time
$e_w$ Thickness field of a vascular wall (i.e. aneurysms and branches)
$e_b$ Thickness field of the branches walls

**Greek Symbols**

$\Gamma$ Generic three-dimensional contour; boundary of an open surface $S$, $\partial S$, in spatial coordinates
$\Psi$ Strain energy function of a hyperelastic law
$\boldsymbol{\chi}$ Referential coordinates system for the arbitrary Lagrangian-Eulerian description
$\boldsymbol{\omega}$ Mesh velocity of a cell centroid
$\boldsymbol{\xi}$ Lagrangian or material coordinates system
$\kappa$ Bulk modulus

*Corresponding author
*Email addresses:* iago.oliveira@unesp.br (I. L. Oliveira), philip.cardiff@ucd.ie (P. Cardiff), cebaccin@gmail.com (C.E. Baccin), jose.gasche@unesp.br (J.L. Gasche)

$\lambda$ Stretch of a solid
$\mu^{\mathrm{f}}$ Dynamic viscosity of a fluid
$\nu^{\mathrm{s}}$ Poisson's ratio of a solid
$\rho$ Density
$\boldsymbol{\sigma}$ Cauchy stress tensor

**Subscripts**

99 Indicates the 99th percentile of a distribution
$ab$ Properties of an aneurysm wall due to abnormal hemodynamics
$b$ Variables or properties of the vascular branches
$ia$ Variables or properties of an aneurysm surface

**Superscripts**

0 Variables at the initial instant or the reference configuration
f Used for fluid-related variables
s Used for solid-related variables

## 1. Introduction

Intracranial aneurysms (IAs) are pathological dilatations of the human vascular system normally found in the bifurcations of the cerebral arteries tree. The most common form has a saccular shape, with a prevalence of up to 90 % in the brain arteries [1], being a dangerous disease that may affect up to 10 % of the world's population [2] and with up to 50 % mortality rate, in case of rupture [3, 4]. This pathology has, in the past three decades, been investigated experimentally [5, 6], which, for example, led to the understanding of the importance of hemodynamics on its development, but also numerically through Computational Fluid Dynamics (CFD), which provided detailed information on the hemodynamics [7] — although still being a debatable topic in the clinical practice [8, 9].

Due to the nature of the pathology, better modeling is continuously sought to allow for more reliable numerical simulations, for example, through the use of Fluid-Solid Interaction (FSI) modeling [10, 11], although numerical techniques to solve FSI problems pose challenging numerical difficulties [12, 13]. Additionally, using an FSI strategy employed for patient-specific IA geometries requires the modeling of their wall tissue that also poses difficulties hard to overcome, such as the lack of patient-specific data of the wall thickness, the constitutive behavior of the tissue and its material properties. This is particularly important due to the large variability of the disease.

Previous experimental works showed that IAs walls are more likely to have wall thickness and mechanical and failure properties varying spatially [14, 15]. This local morphology is caused by the natural history of a particular IA [16, 17]. Meng et al. [18], for example, hypothesized two biological pathways, dependent on different local hemodynamic conditions, that would lead to different wall phenotypes — the authors

name these two phenotypes as "type-I", comprising small IAs with thin and translucent walls, and "type-II", encompassing large IAs with thick, white or yellow, atherosclerotic walls. Moreover, a spectrum of morphologies would exist between these broad phenotypes, as investigated by Kadasi et al. [14], for example, who found that 27 % of IAs are type-I, 8 % are type-II, and 65 % contain both patch types.

How a patient-specific IA grows also influences its mechanical behavior, classically considered to be well described by hyperelastic laws [19] — even though particular laws to suitably represent it do not exist [20]. In the last decade, a few works mechanically characterized samples of IA tissue using uniaxial tests to failure, obtaining the values of the material constants that appear in hyperelastic laws classically associated with artery tissue behavior [21]. Typical examples are the Mooney-Rivlin (MR) law [22], the Yeoh law [23], and an isotropic exponential Fung-like quadratic law [24]. Apart from the mechanical constants, other properties of IAs tissue have also been reported by Costalat et al. [22], for example, who found that the tissue of unruptured IAs is stiffer than ruptured IAs tissue. Finally, in possession of IA tissue samples, these works have also measured their average thickness, further confirming that an IA is globally thinner than its surrounding arteries.

Although it is still a challenge to measure the local morphology, i.e. the local wall thickness and tissue material properties, for a large number of patient-specific IAs, some works on the subject exist. Signorelli et al. [15], for example, used an "indentation device" to measure, in a point-wise manner, the elasticity modulus of an IA sac sample with a resolution of 1 $mm^2$. Their findings suggest that the rupture site is less stiff, i.e. with a smaller elasticity modulus than the rest of the sac, where they found that stiff regions were mixed with thinner regions. The technique has the same drawbacks as classical uniaxial tests, though, because it still requires the aneurysm tissue to be collected, hence *in vivo* measurements are unfeasible. In this regard, imaging techniques are thought to be a promising alternative to measuring the local thickness of a patient-specific IA sac, as performed by Kleinloog et al. [25] through an experimental study in which the wall thickness of IAs was measured using a 7T Magnetic Resonance Imaging.

Cebral et al. [26] used CFD to investigate an IA sac's local morphological heterogeneity. The authors subdivided the wall of a sample of IAs into five regions with specific phenotypes: atherosclerotic, hyperplastic, thin, the rupture site, and "normal-appearing" by intraoperative observation and correlated each of them with local hemodynamics. They found a similar relationship between the local hemodynamics conditions investigated by Meng et al. [18], so-called "low-flow" and "high-flow" effects, and the wall phenotypes. Their study is a good example of how numerical simulations could be used to predict the IA sac heterogeneity on a

patient-by-patient basis.

Therefore, accounting for all these modeling requirements makes the modeling of a patient-specific IA wall a challenge due to both the scarce experimental data to feed numerical models and the large variability of the disease, which prevents patient-specific computations. This is reflected in the modeling choices used by the few numerical works that investigated the mechanical response of IAs. For example, in terms of the approach to estimating the wall thickness, we found a majority that employed uniform thickness throughout the IA sac and branches [27, 28, 29, 30], and a small amount that employed a uniform thickness for the aneurysm sac and a different one on the branches [31], or a lumen-diameter thickness [10]. Finally, only a single work obtained the patient-specific thickness distribution of the IA sac [32] and compared it with a whole uniform wall model, nonetheless the authors used micro-computed tomography to scan the aneurysm sac, a technique that is difficult to apply in a larger cohort of IAs.

Regarding the selection of constitutive law, works that numerically solved the FSI problem with patient-specific IA subjects have used several different ones. Surprisingly, we found a majority that has chosen the small-strain Hookean law that, rigorously, should not be used in finite-deformation motions [33, 30, 11, 34]. Other works employed the classic neo-Hookean law [35] or more specialized ones, such as exponential laws [28] and the MR law [36], although in a smaller number, and not always using the material properties of patient-specific IA tissue.

Despite the uncertainty about which law to choose, the assessment of the impact of different material laws on the mechanics of IAs walls has been the subject of even fewer studies. Torii et al. [28] performed FSI simulations for one IA case, by assuming, first, the rigid wall assumption — thus "pure" CFD simulations —, and three elastic laws: the Hookean law (thus, assuming small strains), the St. Venant-Kirchhoff law, and another hyperelastic law using the exponential strain-energy function proposed by Demiray [37]. Their findings showed that the displacement profiles were qualitatively similar among all the elastic laws, although the maximum displacement with the exponential hyperelastic law was 36 % smaller than that for the St. Venant-Kirchhoff law. Unfortunately, their results on the wall mechanics were limited to the displacement field, no stresses or strain were analyzed because their focus was on the hemodynamics.

An earlier trial to assess different constitutive laws in IAs' mechanical response was conducted by Ramachandran et al. [38], with patient-specific IAs geometries. The authors assumed them to be statically determined, i.e. their mechanical response was independent of the material properties, and investigated the impact of different constitutive laws on the wall stresses and strains by numerically simulating only

the aneurysm sac with Computational Solid Dynamics (CSD) by using a numerical modeling similar to inflation experiments. They used both anisotropic and isotropic versions of Fung-like laws, the Yeoh law with three parameters, the St. Venant-Kirchhoff law, and Hooke's law too. Their results suggested that the aneurysm sac may indeed be statically determined regarding different material laws. However, they only studied the aneurysm sac, i.e. they removed the surrounding arteries portions that may have had an impact on the aneurysms sac stresses, and their pressure-inflation model employed static boundary conditions (BCs), which limits their conclusions. Indeed, the authors highlighted that these conclusions may not stand when the full vasculature would be simulated with dynamical BCs that realistically reflect the cardiac cycle forces.

In this current scenario, it is clear that it remains broadly unknown what is the average impact of the use of different hyperelastic laws and wall morphology models in the mechanics of IAs, i.e. in the stress and strain fields of the IA sac. Therefore, the aim of this work was to assess what could be the impact of choosing different material laws and different morphology models to numerically obtain the mechanical response of IAs. More specifically, we investigated whether a wall model with uniform thickness and material constants, for example, would be acceptable to be used, given the dominant heterogeneity existing for this disease. This is essential in investigations of IA rupture while promising tools that could extract the heterogeneity of the wall more accurately are not ready to do that for a large cohort of patient-specific IAs and, also, because ultimately the rupture event depends on the stress and strain levels on the wall.

## 2. Numerical Methodology

### *2.1. Sample Selection and Geometry Preparation*

We selected twelve vascular geometries from digital subtraction angiography (DSA) examinations collected retrospectively. Nine were collected in the Albert Einstein Israelite Hospital, São Paulo, and approved to be used by the institution's Research Ethics Committee as also by the Research Ethics Committee of the Faculty of Medicine of São Paulo State University (UNESP), Campus of Botucatu. The additional three vascular geometries were obtained from the Aneurisk dataset repository [39], which provides a set of IAs geometries used during the Aneurisk project and are available under the "CC BY-NC 3.0" license. We used these additional geometries due to the lack of sufficient ruptured cases in the original dataset to build a representative sample.

The twelve vasculatures harbored thirteen bifurcation IAs, all of them originating from the more common bifurcation spots of IA occurrences in the brain vessels (the internal carotid artery (ICA) and middle cerebral

artery (MCA)). Seven were unruptured and six ruptured with maximum dome diameter ranging from, roughly, 3 mm to 7 mm, thus categorizing them as small- or medium-sized IAs (mean $\pm$ standard deviation equals $4.93 \pm 1.59$ mm for the ruptured group and $6.28 \pm 1.30$ mm for the unruptured group). For reference, they were labeled by appending their rupture status, prefix "r" for ruptured and "ur" for unruptured, to their parent artery. For example, an unruptured case in the ICA bifurcation is labeled "urICA", followed by a natural number in case of repetition.

The DSA images were segmented using the Vascular Modeling Toolkit (VMTK)® library [40] with the level-set segmentation method [41]. The selection of the volume of interest was not defined *a priori* but chosen large enough to ensure that it enclosed only the aneurysm and its closest surrounding vessels. Subsequently, a triangulated surface was generated with the Marching Cubes algorithm [42, 43]. Inlet and outlet profiles were artificially created in the surfaces to impose BCs for the numerical simulations.

### *2.2. Physical and Mathematical Modeling and Boundary Conditions*

In the flow domain, blood was assumed to be a weakly compressible Newtonian fluid flowing in an isothermal laminar regime, hence the continuity, momentum, and an equation of state were solved for the fields of flow velocity, $\boldsymbol{v}^{\mathrm{f}}$, pressure $p^{\mathrm{f}}$, and blood density $\rho^{\mathrm{f}}$. For a moving control volume in the fluid domain, $V^{\mathrm{f}}(t)$, and using the arbitrary Lagrangian-Eulerian (ALE) framework, where the reference coordinate system is given by $\boldsymbol{\chi}$, the continuity equation is written as:

$$\frac{\partial}{\partial t}\Big( \int\limits_{V^{\mathrm{f}}(t)} \rho^{\mathrm{f}} \mathrm{d}V \Big)\Big|_{\boldsymbol{\chi}} + \oint\limits_{S^{\mathrm{f}}(t)} \rho^{\mathrm{f}} \left( \boldsymbol{v}^{\mathrm{f}} - \boldsymbol{\omega} \right) \bullet \boldsymbol{n}^{\mathrm{f}} \mathrm{d}S = 0 \,, \tag{1}$$

where $\boldsymbol{\omega}$ is the velocity of the referential system of the ALE formulation, and $\boldsymbol{n}^{\mathrm{f}}$ is the outward normal vector to the control surface $S^{\mathrm{f}}$; additionally, the momentum equation in integral form is given by:

$$\frac{\partial}{\partial t}\Big( \int\limits_{V^{\mathrm{f}}(t)} \rho^{\mathrm{f}} \boldsymbol{v}^{\mathrm{f}} \mathrm{d}V \Big)\Big|_{\boldsymbol{\chi}} + \oint\limits_{S^{\mathrm{f}}(t)} \rho^{\mathrm{f}} \boldsymbol{v}^{\mathrm{f}} \left( \boldsymbol{v}^{\mathrm{f}} - \boldsymbol{\omega} \right) \bullet \boldsymbol{n}^{\mathrm{f}} \mathrm{d}S = \oint\limits_{S^{\mathrm{f}}(t)} \boldsymbol{\sigma}^{\mathrm{f}} \bullet \boldsymbol{n}^{\mathrm{f}} \mathrm{d}S \,, \tag{2}$$

where $\boldsymbol{\sigma}^{\mathrm{f}}$ is the Cauchy stress tensor, given by:

$$\boldsymbol{\sigma}^{\mathrm{f}} = -p^{\mathrm{f}} \boldsymbol{I} + \mu^{\mathrm{f}} \left[ \nabla \boldsymbol{v}^{\mathrm{f}} + (\nabla \boldsymbol{v}^{\mathrm{f}})^{\mathrm{T}} \right] - \frac{2}{3} \mu^{\mathrm{f}} \left( \nabla \bullet \boldsymbol{v}^{\mathrm{f}} \right) \boldsymbol{I} \,, \tag{3}$$

and $\boldsymbol{I}$ is the second-order identity tensor. Blood dynamic viscosity was assumed to be $\mu^{\mathrm{f}} = 3.3 \times 10^{-3}\,\mathrm{Pa\,s}$.

Finally, blood compressibility was assumed to be governed by the barotropic equation of state, which has already been used to model the behavior of blood in FSI problems [44, 45, 46]. It can be applied for

liquids at "low pressures" when the change in density is linearly related to the pressure change according to the definition of the bulk modulus of the fluid, $\kappa^{\mathrm{f}}$:

$$\kappa^{\mathrm{f}} = \rho^{\mathrm{f}} \frac{\partial p^{\mathrm{f}}}{\partial \rho^{\mathrm{f}}} \,. \tag{4}$$

In this case, the pressure and the fluid density are related by:

$$\rho^{\mathrm{f}} = \rho_0^{\mathrm{f}} + \frac{\rho_0^{\mathrm{f}}}{\kappa^{\mathrm{f}}} \left( p^{\mathrm{f}} - p_0^{\mathrm{f}} \right) , \tag{5}$$

where the subscript "0" indicates a reference state of the fluid, assumed to be blood at an average cardiac cycle pressure, 100 mmHg, with $\rho_0^{\mathrm{f}} = 1000.0\,\mathrm{kg/m^3}$. Blood bulk modulus was assumed to be $2.2 \times 10^9$ Pa [44].

The solid domain, i.e. the IA and artery walls, was assumed as isotropic and represented by a hyperelastic constitutive law. In the finite-deformation regime, the momentum equation was solved in the total Lagrangian formulation and integral form, written as:

$$\int\limits_{V_0^{\mathrm{s}}} \rho_0^{\mathrm{s}} \frac{\partial^2 \boldsymbol{u}}{\partial t^2}(\boldsymbol{\xi}, t) \mathrm{d}V_0 = \int\limits_{V_0^{\mathrm{s}}} \nabla_0 \bullet \left[ J \boldsymbol{F}^{-1} \bullet (\boldsymbol{\sigma}^{\mathrm{s}} + \boldsymbol{\sigma}_0^{\mathrm{s}}) \right] \mathrm{d}V_0 \,, \tag{6}$$

where $\boldsymbol{u}$ is the motion displacement, $\rho_0^{\mathrm{s}}$ is the tissue density at the reference configuration, and $\boldsymbol{F} = \boldsymbol{I} + (\nabla_0 \boldsymbol{u})^{\mathrm{T}}$ is the deformation gradient of the motion, with $J = \det(\boldsymbol{F})$. The subscript "0" indicates any property or derivative that was evaluated with respect to the coordinates system of the reference configuration, indicated by $\boldsymbol{\xi}$. The reference configuration was assumed to be the domain configuration at the time zero and to be pre-stressed with a Cauchy prestress field calculated by $\boldsymbol{\sigma}_0^{\mathrm{s}} = J^{-1} \boldsymbol{F} \bullet \boldsymbol{S}_0 \bullet \boldsymbol{F}$. The second Piola-Kirchhoff prestress tensor, $\boldsymbol{S}_0$, was computed using the same approach employed by Bazilevs et al. [10].

Finally, the Cauchy stress of the solid, $\boldsymbol{\sigma}^{\mathrm{s}}$, was calculated using three different hyperelastic laws that are defined based on their strain-energy function, $\Psi$, as follows:

- the MR law with 3 material constants [47]:

$$\Psi(I_1, I_2) = c_{10}\,(I_1 - 3) + c_{01}\,(I_2 - 3) + c_{11}\,(I_1 - 3)\,(I_2 - 3)\,; \tag{7}$$

- the Yeoh law with 3 material constants

$$\Psi(I_1) = c_{10}\,(I_1 - 3) + c_{20}\,(I_1 - 3)^2 + c_{30}\,(I_1 - 3)^3\,; \tag{8}$$

- and an "isotropic" version of the exponential Fung-like law, originally proposed by Demiray [37]:

$$\Psi(I_1) = \frac{k_1}{k_2}\left[\mathrm{e}^{\frac{k_2}{2}(I_1-3)} - 1\right], \tag{9}$$

where $I_1$ and $I_2$ are the first and second invariants of the right Cauchy-Green deformation tensor. The complete constitutive model employed a volumetric-decomposition approach as explained in Holzapfel et al. [48]. In this framework, the volumetric part of the tissue motion, dependent on the tissue compressibility, was ultimately measured by the Poisson's ratio of the tissue, $\nu^{\mathrm{s}}$ through its bulk modulus, $\kappa^{\mathrm{s}}$, as computed by the linearized theory:

$$\kappa^{\mathrm{s}} = \frac{E}{3(1-2\nu^{\mathrm{s}})}, \tag{10}$$

For the simulations in this work, the Poisson ratio was assumed to be 0.48 — we performed a parametric study of its influence on the stresses and stretch on an IA sac surface and found that by increasing it above 0.48, both average fields over the sac changed by less than 2 %, on average, for all the hyperelastic laws, while still yielding reasonable computational times. The linearized Young's modulus for the hyperelastic laws was also calculated based on the uniaxial deformation, resulting in $E = 6\left(\frac{\partial\Psi}{\partial I_1} + \frac{\partial\Psi}{\partial I_2}\right)$ [49].

*Boundary conditions (BCs)*

At the flow inlet (see Fig. 1), a time-varying pulsatile velocity profile was imposed varying spatially according to the fully-developed laminar flow in a pipe:

$$\boldsymbol{v}^{\mathrm{f}}_{inlet}(r,t) = 2\frac{\bar{q}_a(t)}{A_{inlet}}\left[1 - \frac{4r^2}{{d_a}^2}\right], \tag{11}$$

where $A_{inlet}$ is the cross-sectional area of the inlet artery, $d_a$ is its diameter, and $r$ is the radial coordinate of the circular inlet section — an artificial circular-section extension, with a length equal to twice the diameter $d_a$, was added to the artery inlet to impose this inlet flow condition. The blood flow rate, $\bar{q}_a(t)$, corresponding to the flow pulse from the beginning of systole until the end of the diastole, was obtained by multiplying the normalized flow rate reported by Hoi et al. [50], for older adults, by the mean blood flow rate in the respective IA parent artery reported by Zarrinkoob et al. [51]. This population-averaged rate was employed because the patient-specific blood flow rate waveform at the ICA was not available. An example of the profile used for IAs on the ICA is shown in Fig. 2a. Moreover, the pressure gradient was set to zero at the inlet.

At the outlets, a flux-corrected velocity and a resistance BC for pressure were imposed. The resistance BC is defined as being proportional to the blood flow rate profile, but with levels ranging between the normal

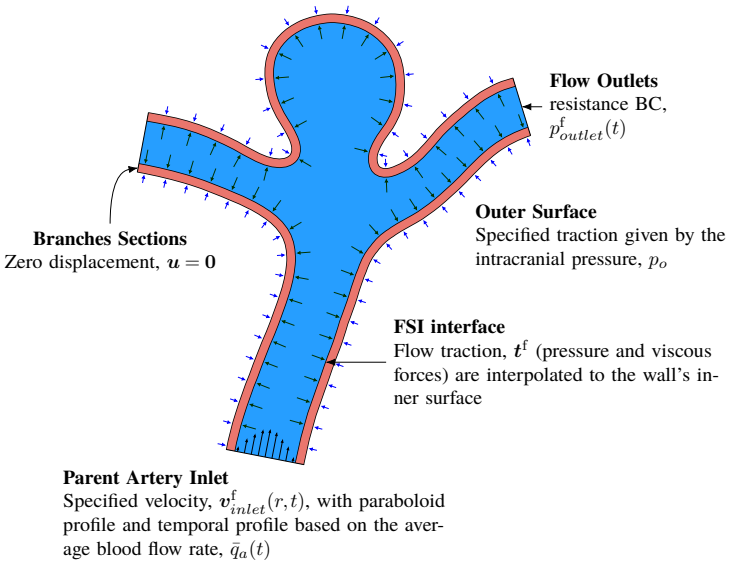


Figure 1: Schematic two-dimensional (2D) representation of the BCs applied in the aneurysms 1WFSI simulations and the domains of artery and IA wall tissue and blood flow.

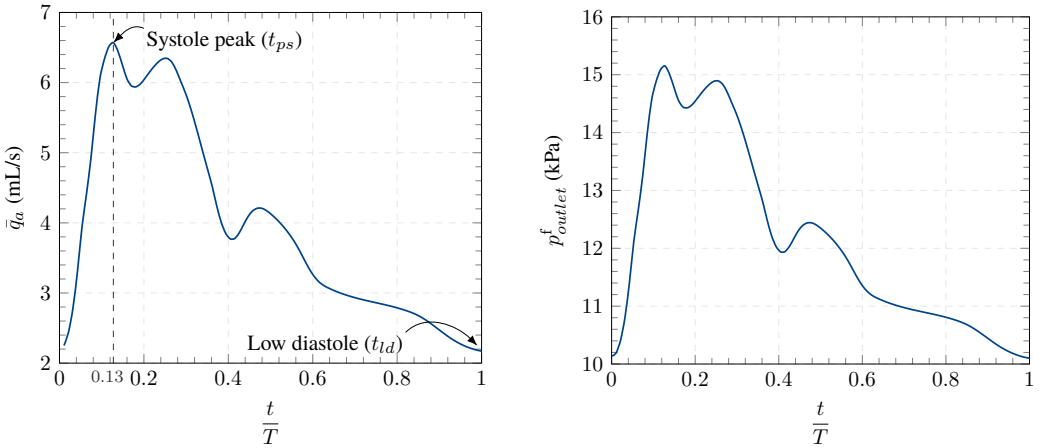


(a) (b)

Figure 2: (a) Flow rate profile waveform for older adults in a cardiac cycle from Hoi et al. [50] (non-dimensional time axis by dividing per the cardiac period, $T = 0.94\,\mathrm{s}$) and (b) pressure waveform used at the flow outlets computed as being proportional to the flow rate and between the normal range 80 to 120 mmHg.

cardiac cycle pressure levels, i.e. from 80 to 120 mmHg (approximately 10 to 15 kPa, see Fig. 2b). Since the distances between the outlets and the aneurysm were not sufficiently long and we did not add cylindrical extensions at the outlets to avoid large computational meshes, reports show that it is important to use this BC [52].

On the outer surface of the solid wall (the abluminal surface), a pressure of $p_o = 5\,\mathrm{mmHg}$, corresponding to the intracranial pressure, was imposed. Although the intracranial pressure seems to vary among patients,

we have found similar values in related studies [53, 36]. On branch "sections" that were artificially created due to the segmentation process (indicated in Fig. 1), we imposed zero displacements, i.e.:

$$\boldsymbol{u} = \mathbf{0}\,. \tag{12}$$

### *2.3. Modeling the Heterogeneity of the IA Wall*

The modeling of the thickness, $e_{ia}$, and material constants of the IA sac wall — represented here as $c_{ij}$ as they correspond to the constants appearing in the laws given by Eqs. (7) to (9) — will be referenced as "wall morphology modeling" and two approaches were employed. In the *uniform-wall model*, we assumed that both $e_{ia}$ and $c_{ij}$ were uniform over the IA sac, while in the abnormal-wall model we assumed that the two wall properties' distributions are governed by the adjacent time-averaged wall shear stress (TAWSS) and oscillatory shear index (OSI) fields of the intra-aneurysmal flow. Both approaches used the same modeling for the IA's surrounding branches.

Computationally, both were built with scripts in VMTK® and an in-house code based on the Visualization Toolkit (VTK)®. The thickness field defined by each model was used to build the computational mesh of the solid domain (see Section 2.4), whereas the material constants fields were computationally created in these meshes. The starting point was the manual delineation of the *neck contour*, over the triangulated surface extracted from the DSA exams, by interactively marking its path. Mathematically, the neck contour or path, $\Gamma_{ia}$, separates the surface of the branches, $S_b$, from the IA sac, $S_{ia}$ (see Fig. 3 for a schematic example of $\Gamma_{ia}$ and other terms used in this section).

#### *Morphology of the Branches Wall*

The thickness of $S_b$, $e_b$, was based on established evidence that arteries thickness is dependent on the vessel lumen diameter [54] and used the wall-to-lumen ratio (WLR) [55] to estimate the branch thickness. The WLR is defined as $WLR \equiv \dfrac{\text{artery wall thickness}}{\text{artery lumen diameter}} = \dfrac{e_b}{d_l}$, where $d_l$ is the artery lumen diameter at a specified position along the vasculature. Therefore, the local branch thickness was calculated as $e_b(\boldsymbol{\xi}) = WLR \times d_l(\boldsymbol{\xi})$ (note that $e_b$ was defined at the reference configuration, hence defined in material coordinates, $\boldsymbol{\xi}$).

The lumen diameter of each geometry was estimated by using VMTK®, by computing the distance between the vasculature *centerlines* and its surface [41]. Empirical values of the WLR in the cerebral arteries were reported by Nakagawa et al. [55] and used to define a functional form of WLR according to the lumen

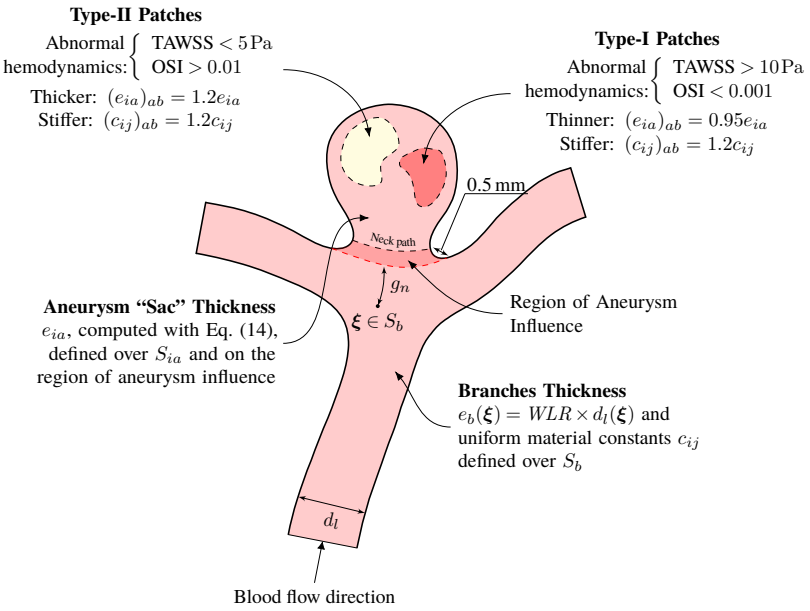


Figure 3: Schematic illustration of the morphology model's components used in this work: the branches surface, $S_b$, has a lumen diameter-dependent thickness and uniform material constants; with the uniform-wall model, the aneurysm sac has a "sac" uniform thickness and material constants, while with the abnormal-wall model, this prior uniform assumption was changed according to "abnormal-hemodynamics" patches defined based on the local TAWSS and the OSI.

diameter, as follows:

$$WLR = \begin{cases} 0.070 & d_l < 2\,\mathrm{mm} \\ 0.070 + 0.018\,(d_l - 2) & 2\,\mathrm{mm} < d_l < 3\,\mathrm{mm} \\ 0.088 & d_l > 3\,\mathrm{mm} \end{cases} . \tag{13}$$

*Uniform-wall model*

We estimated the uniform thickness of the IA sac, $e_{ia}$, as a weighted average of the surrounding branches thickness field, $e_b(\boldsymbol{\xi})$ as follows:

$$e_{ia} = f_a \frac{\int_{S_b} g_n(\boldsymbol{\xi}) e_b(\boldsymbol{\xi}) \mathrm{d}S_b}{\int_{S_b} g_n(\boldsymbol{\xi}) \mathrm{d}S_b} , \tag{14}$$

where $f_a$ is a factor to control how much thinner the aneurysm wall was compared to the vasculature; $f_a = 0.75$ was used consistently for all geometries, consequently $e_{ia}$ was within the range that agrees with measured values available in the literature. The weight function, $g_n$, was the minimum *geodesic* distance between each point of the surrounding branches, $S_b$, and the line that separates the sac and what was named the *region of aneurysm influence* (see Fig. 3). This line may not be coincident with the aneurysm *neck contour*, because, depending on its morphology and location, there might exist regions that neither belong to

the healthy vasculature nor the aneurysm sac. Therefore, it may be imagined as a separation between the *hypothetical healthy vasculature* and the region of aneurysm influence. This line was computed automatically as being 0.5 mm apart from the neck contour.

Finally, the computational procedure used to build these fields created a discontinuity between the thickness on $S_{ia}$ and the branches thickness distribution defined over $S_b$. To correct this biologically unrealistic discontinuity, the resulting thickness was smoothed out using the array smoothing script provided by VMTK® with 15 iterations.

We assumed the material constants, $c_{ij}$, as uniform on both $S_b$ and $S_{ia}$, but with different values according to rupture status, following experimental evidence that ruptured IAs are less stiff than unruptured ones. Hence, the values for each constant (see Table 1) were based on averages of experimental data, with ruptured and unruptured IA, provided by Costalat et al. [22] for the MR law and Brunel et al. [23] for the Yeoh law. We were not able to find any work that fit mechanical data of IA tissue to the isotropic Fung law, hence we based the values used here on the constants used by Torii et al. [56], $k_1 = 0.3536\,\mathrm{MPa}$ and $k_2 = 16.7$, based on experiments with porcine carotid arteries. See Fig. 4a for an example of the resulting fields of $e_w(\boldsymbol{\xi})$ and $c_{10}(\boldsymbol{\xi})$.

Table 1 – Material constants selected for arteries branches, $S_b$, and the IA sac, $S_{ia}$, according to rupture status based on experimental works by Costalat et al. [22] and Brunel et al. [23], for the material laws employed here.

| Law | Constant | $S_b$ | $S_{ia}$ | |
|---|---|---|---|---|
| | | | Ruptured | Unruptured |
| MR | $c_{10}$ (MPa) | 0.1966 | 0.19 | 0.19 |
| | $c_{01}$ (MPa) | 0.0163 | 0.026 | 0.023 |
| | $c_{11}$ (MPa) | 7.837 | 1.377 | 11.780 |
| Yeoh | $c_{10}$ (MPa) | 0.1067 | 0.07 | 0.12 |
| | $c_{20}$ (MPa) | 5.1602 | 2.10 | 6.80 |
| | $c_{30}$ (MPa) | 0.0 | 0.0 | 0.0 |
| Fung | $k_1$ (MPa) | 0.3536 | 0.1768 | 0.7072 |
| | $k_2$ (-) | 16.7 | 16.7 | 16.7 |

*Abnormal-wall model*

We selected two "abnormal-hemodynamics" conditions adjacent to the aneurysm wall that were already associated with phenotypic changes, more specifically, with type-I and type-II regions as proposed by Meng et al. [18]. The type-I phenotype is more likely to be caused by the occurrence of high TAWSS, $> 10\,\mathrm{Pa}$, and low OSI, $< 0.001$ ("high-flow" effects) and cause local wall thinning and stiffening. On the other hand, the

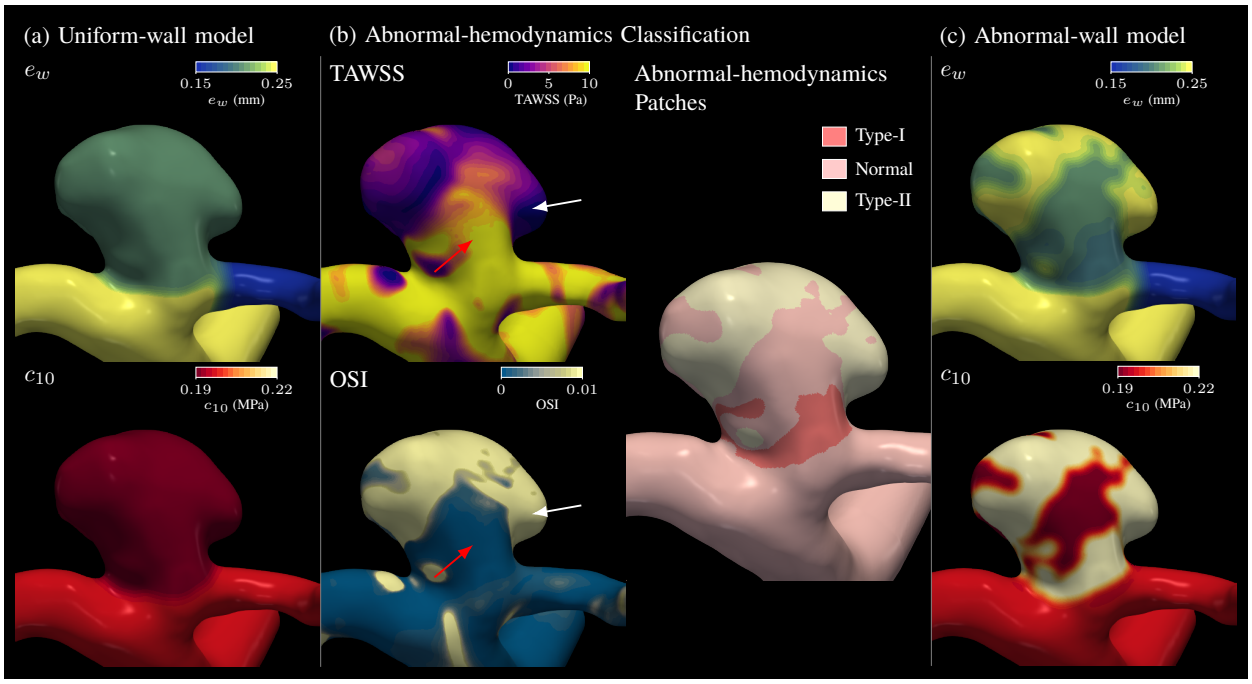


Figure 4: Example of the morphology models construction for an example of a ruptured IA case: (a) Thickness and material constant ($c_{10}$ as an example) fields defined *a priori* on each IA for the uniform-wall model; (b) identification of abnormal-hemodynamics patches on the IA sac surface: TAWSS and OSI fields over the vasculature computed with CFD simulations of the blood flow (left); the red and white arrows point to examples of regions where abnormal hemodynamics occur and identification of the aneurysm sac patches with abnormal hemodynamics (right); "normal" are patches that are neither type-I nor type-II. (c) Finally, fields of thickness and $c_{10}$ resulted by accounting for abnormal intra-aneurysmal hemodynamics (see Fig. 3 too).

type-II phenotype is more likely to be caused by disturbed flow characterized by low TAWSS, $< 5\,\mathrm{Pa}$, and high OSI, $> 0.01$ ("low-flow effects"), causing local stiffening and thickening with atherosclerosis. Those specific thresholds for TAWSS and OSI were chosen based on the averaged values reported by Furukawa et al. [57] and Cebral et al. [26].

For each patient-specific IA geometry, these regions were identified after performing CFD simulations using the rigid-wall assumption — the specific methodology of these simulations can be found elsewhere [58]. The TAWSS and OSI were computed and the identification of the abnormal-hemodynamics patches was performed automatically by using an in-house code implemented with the VTK® library (see Fig. 4b). Patches that were neither identified as type-I or II were labeled "normal".

The fields of aneurysm thickness, $e_{ia}$, and of each material constants on $S_{ia}$ were computationally "updated" according to the illustration in Fig. 3. If a portion of the aneurysm is identified as a type-I patch, the thickness was decreased by 5 % and the material constants were increased by 20 %. On type-II patches, both thickness and material constants were increased by 20 %. The properties on normal patches remained

unaltered, i.e. with the same properties as defined in the uniform-wall model (see Fig. 4c). Finally, these fields were also smoothed to avoid unrealistic discontinuities introduced during the computation procedure.

### *2.4. Computational Meshes and Numerical Strategies*

The numerical simulations were performed in solids4foam [59], an extension of the foam-extend library [60, 61], version 4.0, which uses the second-order-accurate Finite Volume Method (FVM) as the discretization method. The one-way fluid-solid interaction (1WFSI) solution strategy implemented in solids4foam was used, in which the blood flow is first solved assuming a rigid wall and, at each time-step, the wall traction forces are applied as the driving force of the wall motion, whereas the solid deformation is not passed back to the fluid domain. This strategy was chosen to avoid the numerical instabilities that arise in the numerical solution of flow in arterial geometries. That allowed us to simulate a relatively large number of patient-specific IA geometries. Furthermore, in this work we were interested in the mechanical response of the wall, hence only simulating it with the blood flow forces is sufficient for this comparative analysis.

The discretized version of the Eq. (6), with the different hyperelastic laws and morphology models, was solved by using the *segregated* algorithm in solids4foam, while the flow governing equations were solved with the PISO algorithm [62], adapted for the flow of a compressible fluid. In the solution of both sub-problems, we selected second-order interpolation profiles for the spatial discretization to maintain the second-order accuracy level of the FVM. The central differences scheme was used for all the Laplacian terms, with non-orthogonal and skewness corrections [63]. Particularly for the flow's momentum and pressure equations, the second-order upwind scheme was used for the advective term. Moreover, all the gradients in the equations were discretized with the least-squares scheme. The temporal discretization was performed by using the implicit first-order Euler approach for the solid momentum equation and the implicit second-order Euler approach for the flow's momentum equation. Finally, the normalized residual convergence criteria were: $1 \times 10^{-6}$ for the flow 's pressure equation, $1 \times 10^{-8}$ for the flow's momentum equation, and $1 \times 10^{-9}$ for the outer iterations of the solid's momentum.

The fluid and solid computational meshes were built with the triangulated surfaces extracted with VMTK®. The mesh of the flow domain was generated using the utility `cartesianMesh` provided by foam-extend as part of the cfMesh library. This utility automatically creates polyhedral meshes that are predominantly composed of hexahedral cells, i.e. the interior of the mesh consists of cells close in shape to hexahedra. To fit the curved boundary, the cells adjacent to the wall are, generically, polyhedra with a prismatic boundary-layer-refined region composed of five layers. Subsequently, the FSI interface of this fluid mesh, a quadrilateral surface,

was "re-meshed", i.e. the structure of it was modified to only contain triangular faces by using VMTK®. This re-meshing procedure was necessary because of the possibility of pressure oscillations infecting the solid displacement solution when using quadrilateral cells with the segregated approach and the FVM [64]. The solid mesh was, then, created by extruding that re-meshed surface in the outward direction using VMTK® with the thickness field defined in Section 2.3. Six layers were used in the extrusion.

For the type of fluid meshes used in this work, mesh-sensitivity studies were carried out extensively with different IAs geometries and were not included here. They yielded a volume density of cells in the range of 3000 to 4000 cells/mm$^3$ (an example of this study can be found in Oliveira et al. [58]). This level of refinement was assured for the meshes used in this work. We carried out a separate mesh-independence study of the solid meshes by also using the 1WFSI strategy with three systematically-refined meshes. The result was a mesh with a surface-cells density of approximately 240.0 cells/mm$^2$, with 6 layers of cells along with the thickness. We also carried out a time-step refinement study yielding a time-step of $1 \times 10^{-4}$ s. Finally, two cardiac cycles were solved in each simulation, but only the second one was used for the analysis.

### *2.5. Data Analysis*

*Physical Variables of Analysis And Metrics Employed*

We selected the largest principal Cauchy stress field of the solid wall, $\sigma_1 \equiv \sigma_1^{\mathrm{s}}(\boldsymbol{x}, t_{ps})$ (we drop the superscript "s" henceforth), and its largest principal stretch, $\lambda_1(\boldsymbol{x}, t_{ps})$ (given by the square root of the largest principal value of $\boldsymbol{C}$) as the main subjects of our analysis. Both were taken at the *deformed* configuration at the peak-systole, i.e. $t = t_{ps}$ (see Fig. 2a).

Both fields were analyzed only on the luminal and abluminal sides of the aneurysmal region, i.e. on $S_{ia}^{\mathrm{l}}$ and $S_{ia}^{\mathrm{abl}}$. To perform the statistical analysis, we computed two metrics of the fields. The 99th percentile of each field, $(\sigma_1)_{99}$ and $(\lambda_1)_{99}$, were used as "proxies" of the fields' maximum specifically for the statistical analysis, due to possible mesh-induced differences in the absolute maximum. The second metric was the surface average of a field over a surface, $S$, defined as follows, for $\sigma_1$:

$$\langle \sigma_1 \rangle_S = \frac{1}{A(S)} \int_S \sigma_1(\boldsymbol{x}) \mathrm{d}S, \;\; \boldsymbol{x} \in S \,, \tag{15}$$

where $A()$ is the area operator and $S$ is either $S_{ia}^{\mathrm{l}}$ or $S_{ia}^{\mathrm{abl}}$. For $\sigma_1$, the surface-average metric gives a measure of the total traction on $S$ caused by this stress. A similar physical meaning cannot be said about $\langle \lambda_1 \rangle$ although the same definition was used regardless.

Computationally, the 99th percentile was computed with Python's NumPy library [65], whereas the surface average was computed using an in-house code that computes the integral in Eq. (15) with first-order accuracy

*Statistical Analysis*

Statistical tests were performed with n = 13, for the 99th percentiles and the surface averages, by using the SciPy library [66] with a significance level of $\alpha = 0.05$ (hence, 95 % confidence interval). All distributions were tested for normality by using the Shapiro-Wilk test.

To compare the two wall morphology models, for each hyperelastic law, the paired t-test and the Wilcoxon signed-rank tests were used for normal and non-normal distributions, respectively. Similarly, to compare the three distributions of the hyperelastic laws, the ANOVA test and the Kruskal-Wallis test were used *a priori* for normal and for non-normal distributions, respectively. Subsequently, pair-wise posthoc analyses were performed to test the distributions. The t-test and Dunn's posthoc methods were employed, in this case, for normal and non-normal distributions, respectively, via Python's scikit-posthoc library.

*Relative Comparison Among Different Models*

To quantify the differences among the metrics, we computed the *absolute* differences between the mean of the distributions obtained with each modeling approach. If $\overline{\mathcal{M}}$ is the mean of the distribution of a metric $\mathcal{M}$, for a fixed hyperelastic law, the mean difference between the uniform and abnormal wall morphologies for a sample was defined as:

$$D_{\mathcal{M}}^{\text{WM}} = \left| \overline{\mathcal{M}}_{AWM} - \overline{\mathcal{M}}_{UWM} \right| , \tag{16}$$

where the superscript "WM" stands for "wall morphology", and, consequentely, "UWM" and "AWM" indicate the uniform and abnormal-wall models.

Because three hyperelastic laws were employed and none can be assumed the "gold standard" to represent IA tissue, first, a difference similar to Eq. (16), but in a pair-wise manner between the three laws, MR, Yeoh, and isotropic Fung, was computed. Then, the maximum of these values was found, or mathematically:

$$D_{\mathcal{M}}^{\text{HL}} = \max_{i,j} \left( \left| \overline{\mathcal{M}}_i - \overline{\mathcal{M}}_j \right| \right) , \tag{17}$$

where the superscript "HL" stands for "hyperelastic laws" and the pair $(i, j)$ assumes the values in the set of permutations among the three hyperelastic laws.

## 3. Results

A preliminary qualitative analysis of the $\sigma_1$ and $\lambda_1$ fields in two representative cases of the ruptured and unruptured groups (labeled from now on as $\mathcal{R}$ and $\mathcal{U}$, respectively), namely, cases rMCA1 and urICA1 suggests that the different hyperelastic laws exert less influence on $\sigma_1$ than on $\lambda_1$ and this seems to be true for both IAs (see Fig. 5). The $\lambda_1$ field in case rMCA1 has a different overall magnitude on its sac depending on the law, whereas the qualitative differences in urICA1 are less apparent (see on the top panel of Fig. 6 how the Fung and Yeoh laws produce higher levels of stretch in much larger areas than the MR law). On the other hand, for both $\sigma_1$ and $\lambda_1$, the two morphology models produce similar fields, regardless of the particular hyperelastic law or the rupture status. Similar trends were found when inspecting the abluminal surface, $S_{ia}^{\mathrm{abl}}$.

These two IA cases were chosen as representative examples because they yielded the largest absolute difference $D_{\mathcal{M}}^{\mathrm{HL}}$ in the groups $\mathcal{R}$ and $\mathcal{U}$, respectively. Nevertheless, the patterns indicated by them seem to be examples of larger trends. By comparing the sample's distributions for the three hyperelastic laws (see Fig. 7), $\sigma_1$'s metrics did not reach statistical significance ($p = 0.73$ and $p = 0.57$, with the uniform-wall model and abnormal-wall model, respectively, for $\langle \sigma_1 \rangle_{S_{ia}^{\mathrm{l}}}$ ; similar values were found for $(\sigma_1)_{99}$). Furthermore, a posthoc analysis using the t-test in a pair-wise manner yielded that the three distributions are not significantly different (p-values depicted in Fig. 7 with the symbol "$\circ\cdots p\cdots\circ$", for the abnormal-wall model only; similar p-values were found with the uniform-wall model).

The opposite was the case for the distribution of $\lambda_1$'s (Fig. 8), in which case the three distributions were significantly different ($p = 0.033$ with the uniform-wall model and $p = 0.026$ with the abnormal-wall model for $\langle \lambda_1 \rangle_{S_{ia}^{\mathrm{l}}}$ , with similar values found for $(\lambda_1)_{99}$). Nevertheless, a posthoc analysis, using Dunn's test, indicated that only the differences between the pairs (MR, Yeoh) and (MR, Fung) were indeed significant (see p-values below the plots in Fig. 8).

Furthermore, the different behavior of $\lambda_1$ between the ruptured and unruptured cases evidenced above is part of a trend by noting a visible and consistent "separation" of $\lambda_1$ levels according to rupture status (see the data points in Fig. 8), independently of hyperelastic law or morphology model. That gap is the largest for the isotropic Fung law, explaining the large dispersion of the distributions of $\lambda_1$'s metrics, although the same can also be perceived with the Yeoh and MR models, to a smaller extent. This particular feature did not occur for $\sigma_1$'s metrics — note that they spread over a range between, approximately, 0.15 MPa to 0.30 MPa but are not visibly segregated by rupture status (see the data points in Fig. 7).

By comparing the distributions between the uniform-wall model and abnormal-wall model, they reached

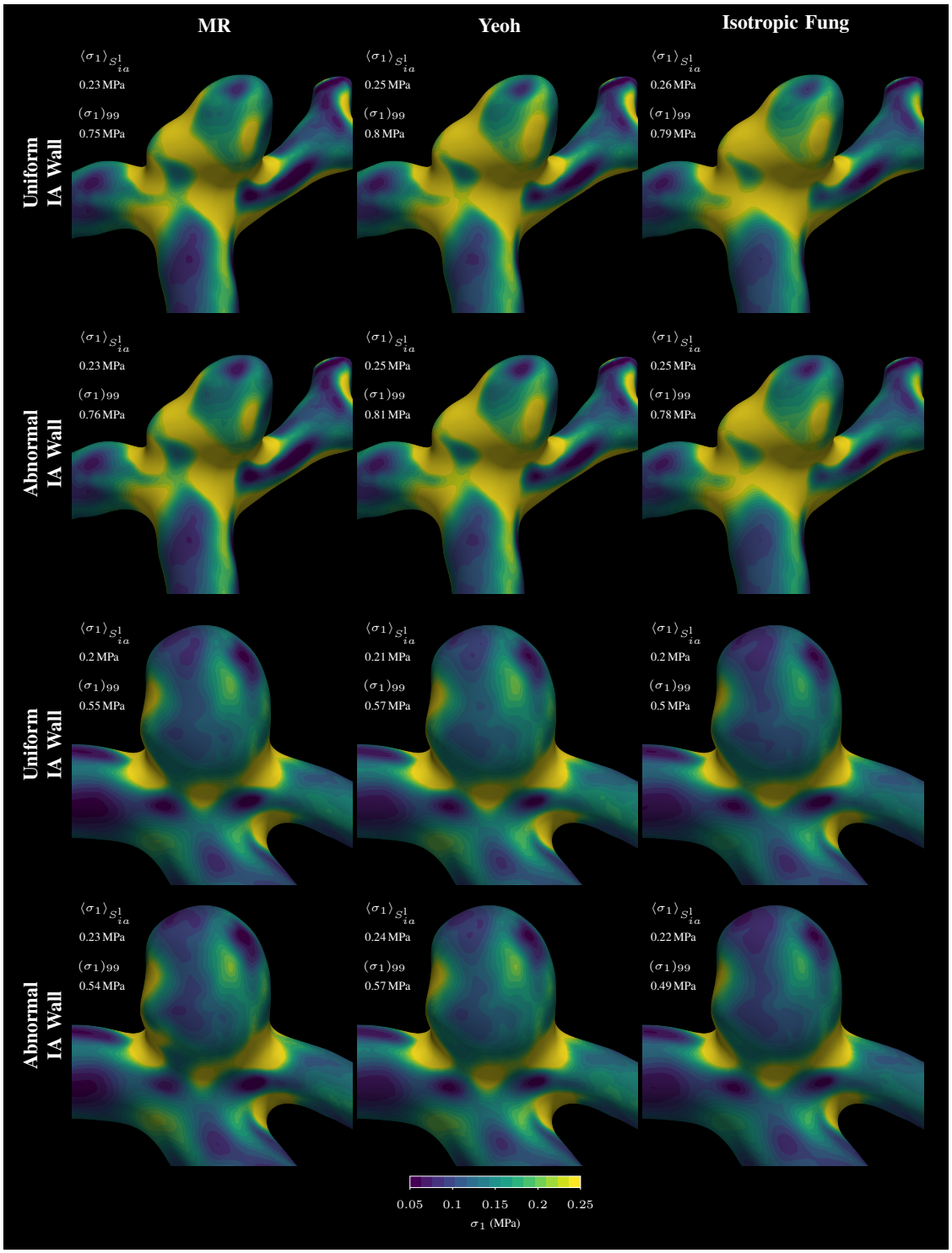


Figure 5: Largest principal Cauchy stress, $\sigma_1$, at the peak systole, on $S^1_{ia}$, for cases rMCA1 (top panel) and urICA1 (bottom panel), with different hyperelastic laws (columns), and wall morphology models (rows).

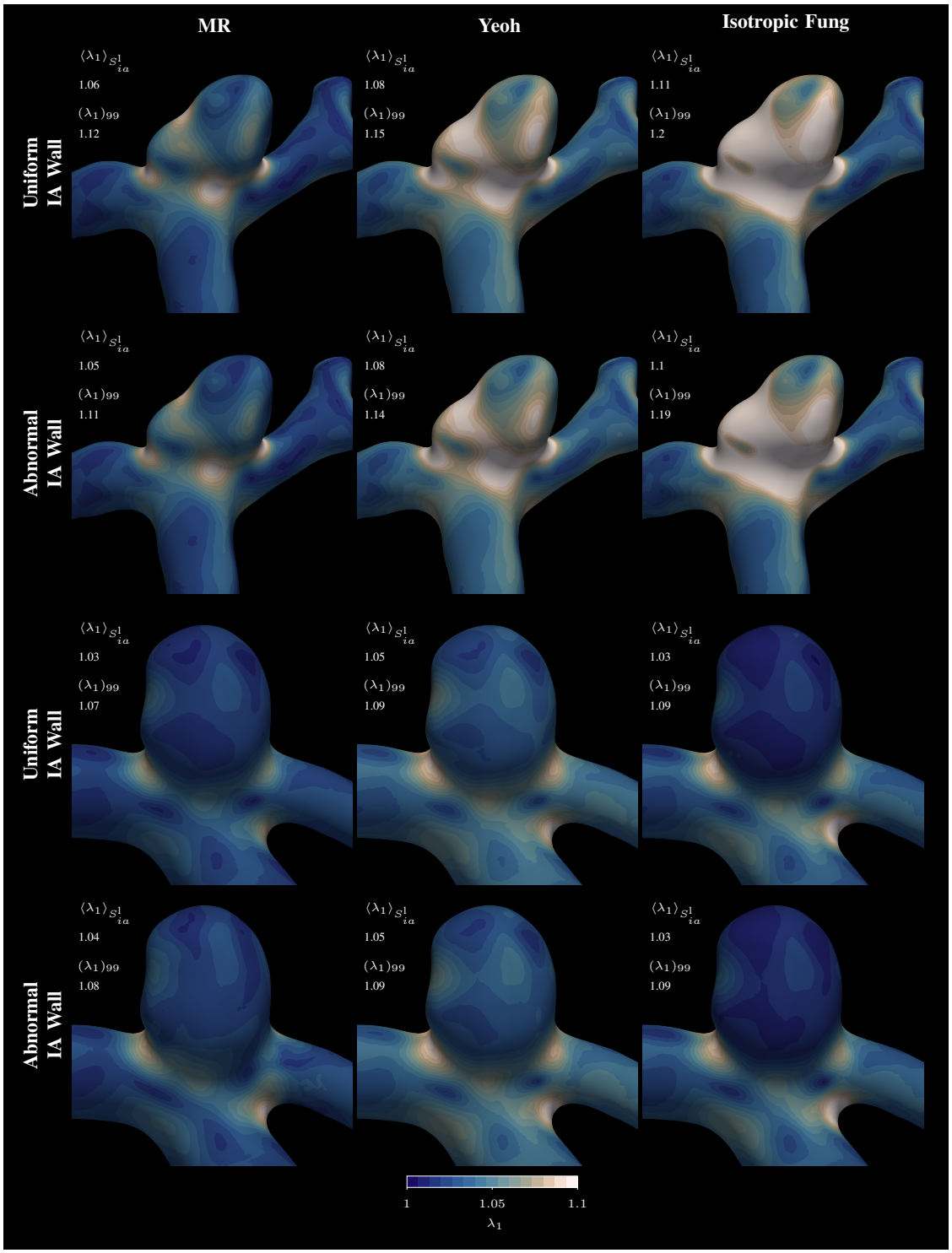


Figure 6: Largest principal stretch, $\lambda_1$, at the peak systole, on $S^1_{ia}$, for cases rMCA1 (top panel) and urICA1 (bottom panel), with different hyperelastic laws (columns), and wall morphology models (rows).

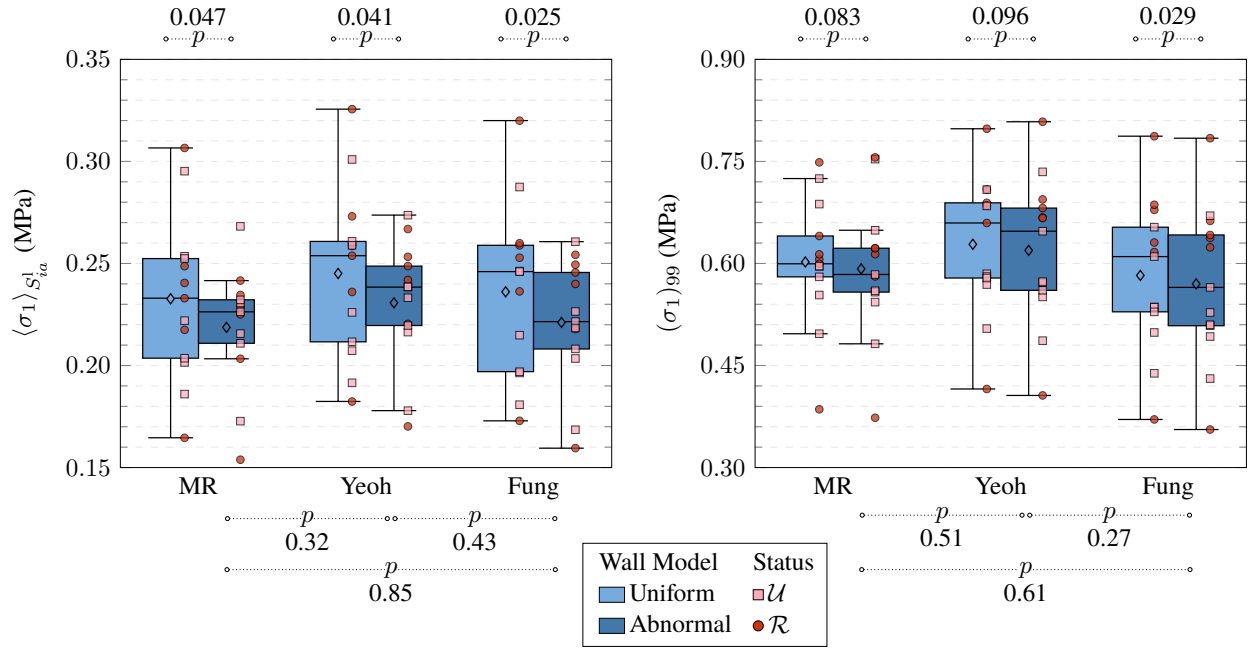


Figure 7: Box plots and data points (placed on top of their respective box plot) of the distributions of $\langle\sigma_1\rangle_{S^1_{ia}}$ (left) and $(\sigma_1)_{99}$ (right) for the IA sample simulated with the three hyperelastic laws (along the x-axis) and segregated by morphology model and rupture status. The diamond shape indicates the mean of each distribution. The p-values resulting from hypothesis tests comparing the distributions are shown below and above the plot's area through the special symbol where the two circles visually indicate the two distributions that were compared and the resulting p-value.

statistical significance for both $\lambda_1$ metrics, irrespective of the hyperelastic law (see the p-values above the plots of Fig. 8). The same did not occur for the $\sigma_1$, for which statistical significance was only reached by $\langle\sigma_1\rangle$'s distributions with all laws, whereas the distribution of $(\sigma_1)_{99}$ was only reached for the Fung law.

The absolute differences between the means of $\sigma_1$ and $\lambda_1$ were larger when the hyperelastic laws were compared than when comparing the wall morphology models (Table 2), especially on the luminal surface and irrespective of the morphology model, confirming that the mechanical response is more sensitive to the choice of hyperelastic law. More specifically, it is possible to note that the influence of the hyperelastic laws is more drastic for $\lambda_1$ and depends on the rupture status — note how the mean absolute difference is larger for the ruptured group than the unruptured one in Table 2. Finally, as verified above, that difference for $\lambda_1$ reached statistical significance, whereas it did not with $\sigma_1$.

It is important to note that similar plots of Figs. 7 and 8 were inspected for the metrics calculated on the abluminal surface and the same trends were found (as also indicated by Table 2). This suggests that the trends reported here occur on the whole wall of the IA.

Finally, it is important to note that we performed the same analysis presented above for the $\sigma_1$ and $\lambda_1$

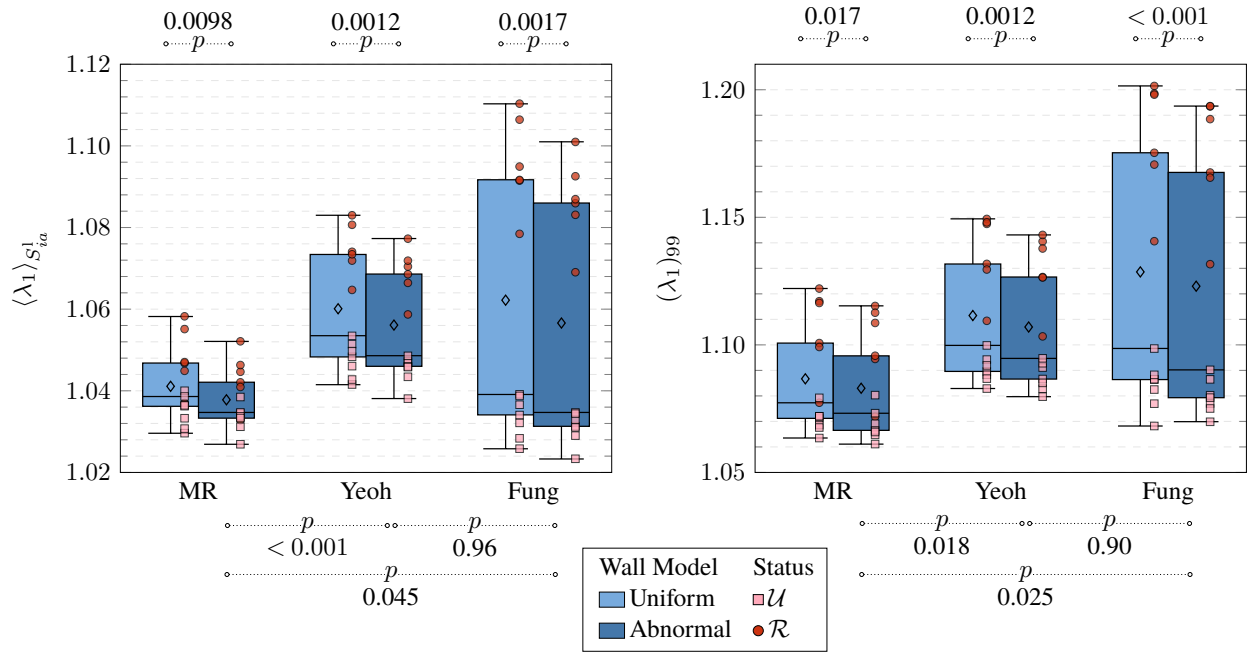


Figure 8: Box plots and data points (placed on top of their respective box plot) of the distributions of $\langle\lambda_1\rangle_{S^1_{ia}}$ (left) and $(\lambda_1)_{99}$ (right) for the IA sample simulated with the three hyperelastic laws (along the x-axis) and segregated by morphology model and rupture status. The diamond shape indicates the mean of each distribution. The p-values resulting from hypothesis tests comparing the distributions are shown below and above the plot's area through the special symbol where the two circles visually indicate the two distributions that were compared and the resulting p-value.

Table 2 – Maximal absolute difference for the selected metrics (surface average and 99th percentile) of the $\sigma_1$ and $\lambda_1$ fields on different surfaces of the IA wall, among the set of pair-wise comparisons of the different hyperelastic laws used for both wall morphology models (Eq. (17)). The differences were averaged over each rupture-status group.

| Side | Field Metric, $\mathcal{M}$ | $D^{\text{HL}}_{\mathcal{M}}$ | | | | $D^{\text{WM}}_{\mathcal{M}}$ | | | | | |
|---|---|---|---|---|---|---|---|---|---|---|---|
| | | Abnormal | | Uniform | | MR | | Yeoh | | Fung | |
| | | $\mathcal{R}$ | $\mathcal{U}$ | $\mathcal{R}$ | $\mathcal{U}$ | $\mathcal{R}$ | $\mathcal{U}$ | $\mathcal{R}$ | $\mathcal{U}$ | $\mathcal{R}$ | $\mathcal{U}$ |
| $S^{\text{l}}_{ia}$ | $\langle\sigma_1\rangle$ (kPa) | 19.1 | 12.9 | 19.8 | 12.6 | 20.6 | 8.25 | 21.3 | 8.49 | 22.4 | 8.79 |
| | $(\sigma_1)_{99}$ (kPa) | 59.3 | 60.6 | 60.4 | 61.9 | 4.23 | 15.1 | 5.28 | 12.2 | 10.8 | 13.7 |
| | $\langle\lambda_1\rangle$ ($\times 10^{-3}$) | 43.3 | 14.2 | 47.4 | 14.1 | 5.03 | 1.74 | 5.74 | 2.47 | 9.12 | 2.60 |
| | $(\lambda_1)_{99}$ ($\times 10^{-3}$) | 73.6 | 18.9 | 75.3 | 19.9 | 5.72 | 1.90 | 6.30 | 2.94 | 7.40 | 4.17 |
| $S^{\text{abl}}_{ia}$ | $\langle\sigma_1\rangle$ (kPa) | 3.79 | 3.49 | 4.79 | 4.06 | 6.28 | 6.51 | 6.71 | 7.97 | 7.70 | 9.35 |
| | $(\sigma_1)_{99}$ (kPa) | 8.90 | 55.2 | 6.74 | 46.9 | 0.124 | 6.16 | 1.86 | 13.2 | 4.01 | 14.4 |
| | $\langle\lambda_1\rangle$ ($\times 10^{-3}$) | 37.1 | 12.2 | 40.3 | 12.3 | 3.06 | 1.47 | 4.07 | 2.24 | 6.27 | 2.17 |
| | $(\lambda_1)_{99}$ ($\times 10^{-3}$) | 62.6 | 14.8 | 64.9 | 17.1 | 4.45 | 0.647 | 5.05 | 2.93 | 6.82 | 3.87 |

fields but taken at the instant of low diastole, $t_{ld}$ (see Fig. 2a), and in general the same trends still hold for the $\sigma_1$. Regarding $\lambda_1$'s metrics, the same trends above hold too, although the values of the absolute differences

between the models tend to decrease uniformly. These trends can be perceived by inspecting $\langle\sigma_1\rangle$ and $\langle\lambda_1\rangle$ along a cardiac cycle in Fig. 9, where it is clear that the largest differences among the models occur near the peak-systole and any difference tends to decrease after the systolic period towards the diastolic period. The large differences among the hyperelastic laws during the systole probably occur as a manifestation of the nonlinearities of the modeling depending on the level of forces driving the motion, which are higher during the systole.

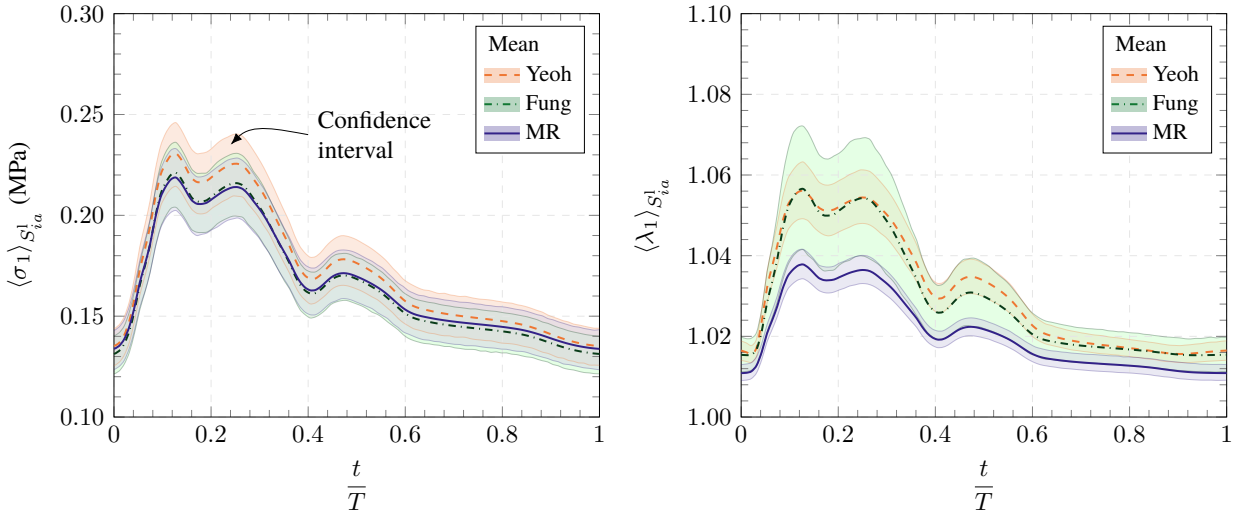


Figure 9: Central tendency plots (mean and confidence interval based on the 95-percentile) along a cardiac cycle (dimensionless time, normalized by the cardiac period $T$) of $\langle\sigma_1\rangle$ and $\langle\lambda_1\rangle$ and $\lambda_1$, computed over $S^1_{ia}$, for the whole IA sample for the three hyperelastic laws and the abnormal-wall model.

## 4. Discussion

The use of numerical simulations to study IAs has increased substantially in the last two decades, although the majority of the works were focused on the hemodynamics inside the IA [4], thus primarily using CFD as their main computational tool. Investigations on the hemodynamics were helpful to a more complete understanding of the role played by the blood flow in an IA's natural history [67]. Nevertheless, investigations on the mechanical response of IA geometries under physiologically realistic conditions, which seems to account for a small percentage of all the works on the subject, are of foremost importance and can be helpful to further understand both their mechanics and, more importantly, the rupture event, which is ultimately a phenomenon occurring in the wall tissue. As argued in the introduction of this work, the lack of that kind of study is understandable due to the complex modeling requirements to realistically represent a patient-specific IA wall tissue. In this regard, to the authors' knowledge, our study is the first attempt to thoroughly assess the

impact of both hyperelastic laws and wall morphology models — i.e. thickness and material constants — on the mechanical response of IAs with a relatively large population's sample.

We employed a realistic modeling of the wall morphology — what we named the "abnormal-wall model" — and the technique to create it allows for patient-specific prediction of the wall morphology based on the underlying hemodynamics. Nonetheless, our results suggest that the abnormal-wall model predicts a similar mechanical response to a model where the aneurysm wall has uniform thickness and material constants, the uniform-wall model — a common alternative used in previous works when patient-specific data is missing, for example —, with absolute differences smaller than when different hyperelastic laws were compared and consistent for the whole cardiac cycle. These findings indicate that the uniform-wall model may be used to find the mechanical response in populational studies of IAs. Care must be taken, though, depending on the particular application of the numerical results because Cebral et al. [68], for example, using similar modeling to the abnormal-wall model to investigate the rupture site of IAs, found that a wall with both uniform thickness and stiffness was not able to predict the rupture point specifically, compared to models with focal properties changes.

Furthermore, according to our results, when numerically simulating the geometry of an IA, the mechanical response in terms of the stretches, $\lambda_1$, was more sensitive to the constitutive law chosen and, additionally, yielded clear differences between ruptured and unruptured IAs. In that regard, the comparative behavior among each law is most likely to be related to their response given the stiffer material properties of the unruptured group. Therefore, as stiffer an IA tissue is, all laws tend to yield the same, or at least similar, mechanical response, in terms of stresses, whereas as less stiff it is, i.e. closer to a ruptured condition, the MR deviates from both Yeoh and Fung results.

We found few studies that investigated the impact of different modeling choices on the mechanical response of IAs. Torii et al. [28] assessed the impact of different materials laws mainly on the hemodynamics, using a single IA geometry, thus limiting the possibility of comparison with our results (regarding the wall motion the authors only reported the maximum displacement on the IA sac and only used one law that we also employed, the Fung law). Ramachandran et al. [38] also directly compared different material laws in patient-specific IA geometries, although they assumed static BCs and simulated only the IA sac, i.e. without the branches walls. They employed anisotropic and isotropic versions of the Fung law, the Yeoh law, and both small and finite strain versions of Hooke's law. Although the material constants they have employed were different, their conclusions broadly agree with the findings in this work, i.e. that the material laws predicted

similar responses in terms of the wall stresses. Although, it is important to note that their study did not use the MR law, the one that presented the most divergent response compared to the Yeoh and Fung responses. The authors recognized, though, that their results could not hold as more patient-specific modeling features were added to the whole IA wall model in populational studies by avoiding the "uniform modeling choices applied across the patient population". The comparison performed here between the uniform-wall model and abnormal-wall model suitably addresses their concerns by showing that the absolute differences between a uniform wall IA and a realistic one, in terms of their mechanical response as given by $\sigma_1$ and $\lambda_1$, are smaller than when comparing different material laws.

From a practical perspective, by assessing the impact of different materials laws and morphology models, suitable modeling can be chosen depending on the particular goals of the simulations. In large cohort studies, for example, simpler models could be used to assess average quantities over the IAs sacs, while keeping the computational times low — for example, the Yeoh law yielded the fastest results while the uniform-wall model and abnormal-wall model yielded similar computational times.

*Limitations*

There exist some controversy on the BCs applied on the artificial sections of the vascular branches because it is difficult to predict which numerical BC can be realistically applied in there. The majority of works we found that have simulated CSD or FSI in vascular geometries commonly employed zero-displacements too [11, 53], although a few [10] applied a BC that allows the arterial branch to slide along the section's tangential direction, but constrains the displacement along with its normal — hence a "zero-shear traction" BC. We performed a numerical study comparing both and found that, although the displacement field was affected by different BCs, both $\sigma_1$ and $\lambda_1$ were unaltered on the aneurysm sacs, with qualitative differences on these fields only near the locations of the sections, as expected. Furthermore, we found that the sections should be made at least two local diameters away from the IAs neck lines to safely assume that the zero-displacement BC would not influence the stress and stretch distribution on the IA. For all the geometries used here, this length was assured for all the branches, including the parent artery.

Additionally, it is important to note that we only employed isotropic laws, despite the tissue of arteries and IAs being anisotropic, based on evidence that anisotropic laws yield similar mechanical responses compared to their isotropic versions [38], although it is important to further confirm that in larger studies.

The values by which thickness and material constants were altered in the assumptions made for the abnormal-wall model (see Fig. 3) were somewhat arbitrary, even if based on scarce data available in the

literature on this subject. For example, we could not find quantitative data on how much thinner the type-I patches are compared to normal walls. In atherosclerotic walls, hence type-II patches, data gathered by Holzapfel and Ogden [69], based on earlier studies, show that arteries with atherosclerotic plaques can be up to 1.5 times thicker than when they are healthy. Similarly, their elastic modulus can be 4 times larger in the later stages of plaque development and in the presence of calcification, but much smaller than 1.5 times in earlier stages. Due to this lack of data, the factors that correctly represented the histological observations for each patch were selected and used consistently among all geometries. Nevertheless, we carried out a parametric study by incrementally changing these scale factors of thickness and material constants separately on type-I and type-II patches (see supplementary material). By then computing $\langle \sigma_1 \rangle_{S^1_{ia}}$ and $\langle \lambda_1 \rangle_{S^1_{ia}}$, we found a mean maximum absolute difference of 20.9 kPa and $5.47 \times 10^{-3}$, respectively, computed between the extremes of the parametric intervals, when the thickness of type-II patches was varied — all the other yield smaller differences. Most importantly, the variation induced by focal changes in thickness and material constants were consistent among all IAs, as expected, therefore our main conclusions would likely withstand if other scale factors were chosen.

Finally, a further limitation was due to the use of the 1WFSI numerical strategy that ignores the two-way coupling between the fluid and solid domains. Nevertheless, given the comparative nature of this work, it is sufficient to set a baseline modeling for all cases simulated, in such a way that a "full" two-way fluid-solid interaction modeling would alter the $\sigma_1$ and $\lambda_1$ consistently and, thus not altering our main conclusions.

## 5. Conclusions

The challenges involved in the experimental acquisition of mechanical properties of patient-specific IAs prevent the use of better modeling to study this disease, especially if numerical simulations are to be used to help in this endeavor. This scenario is particularly pressing because a better understanding of the rupture, and eventual prediction of it, passes through the capacity to compute the mechanical response of an IA wall. In this scenario, this study help to assess the likely impact of certain modeling choices on the mechanical response of IAs.

We found that different wall morphology models — i.e. different thickness and material properties — yield smaller absolute differences than when comparing different constitutive laws, in terms of both stress and stretches of the mechanical response. Furthermore, different hyperelastic laws produced significantly different stretch fields, explained by the likely higher sensitivity of stretch to the material constants of the law,

indicating that ruptured aneurysms had much larger stretches than unruptured ones. The same behavior was not encountered for the stress fields in the IA sac. These findings may help future studies to choose more suitable modeling to investigate other aspects of the mechanical response of IAs.

## 6. Acknowledgements

This research was supported by grants 2017/18514-1 and 2019/19098-7 of the São Paulo Research Foundation (FAPESP) (the funder had no involvment in any step of the production of this manuscript). It was also supported by resources supplied by the Center for Scientific Computing (NCC/GridUNESP) of the UNESP (`www2.unesp.br/portal#!/gridunesp`), by ACENET (`www.ace-net.ca`) through Dalhousie University and Compute Canada (`www.computecanada.ca`).

## References

[1] M. R. Diagbouga, S. Morel, P. Bijlenga, B. R. Kwak, Role of Hemodynamics in Initiation/Growth of Intracranial Aneurysms, European Journal of Clinical Investigation 48 (2018) 1–12, doi:\bibinfo{doi}{10.1111/eci.12992}.

[2] The International Study of Unruptured Intracranial Aneurysms Investigators, Unruptured Intracranial Aneurysms - Risk of Rupture and Risks of Surgical Intervention, The New England Journal of Medicine 339 (24) (1998) 1725–1733.

[3] M. H. M. Vlak, G. J. E. Rinkel, P. Greebe, A. Algra, Risk of Rupture of an Intracranial Aneurysm Based on Patient Characteristics: A Case-Control Study, Stroke 44 (5) (2013) 1256–1259, ISSN 00392499, doi:\bibinfo{doi}{10.1161/STROKEAHA.111.000679}.

[4] K. M. Saqr, S. Rashad, S. Tupin, K. Niizuma, T. Hassan, T. Tominaga, M. Ohta, What Does Computational Fluid Dynamics Tell Us about Intracranial Aneurysms? A Meta-Analysis and Critical Review, Journal of Cerebral Blood Flow and Metabolism 0 (0) (2019) 1–19, doi:\bibinfo{doi}{10.1177/0271678X19854640}.

[5] H. Meng, Z. Wang, Y. Hoi, L. Gao, E. Metaxa, D. D. Swartz, J. Kolega, D. D. Swartz, J. Kolega, Complex Hemodynamics at the Apex of an Arterial Bifurcation Induces Vascular Remodeling Resembling Cerebral Aneurysm Initiation, Stroke 38 (2007) 1924–1931, doi:\bibinfo{doi}{10.1161/STROKEAHA.106.481234}.

[6] E. Metaxa, M. Tremmel, S. K. Natarajan, J. Xiang, R. A. Paluch, M. Mandelbaum, A. H. Siddiqui, J. Kolega, J. Mocco, H. Meng, Characterization of Critical Hemodynamics Contributing to Aneurysmal Remodeling at the Basilar Terminus in a Rabbit Model, Stroke 41 (8) (2010) 1774–1782, ISSN 00392499, doi:\bibinfo{doi}{10.1161/STROKEAHA.110.585992}.

[7] L. Liang, D. A. Steinman, O. Brina, C. Chnafa, N. M. Cancelliere, V. M. Pereira, Towards the Clinical Utility of CFD for Assessment of Intracranial Aneurysm Rupture - A Systematic Review and Novel Parameter-Ranking Tool, Journal of NeuroInterventional Surgery 11 (2019) 153–158, ISSN 17598486, doi:\bibinfo{doi}{10.1136/neurintsurg-2018-014246}.

[8] D. F. Kallmes, Point: CFD—Computational Fluid Dynamics or Confounding Factor Dissemination, American Journal of Neuroradiology 33 (2012) 393–398, doi:\bibinfo{doi}{10.3174/ajnr.A2993}.

[9] J. R. Cebral, H. Meng, Counterpoint: Realizing the Clinical Utility of Computational Fluid Dynamics—Closing the Gap, doi:\bibinfo{doi}{10.3174/ajnr.a2993}, 2012.

[10] Y. Bazilevs, M. C. Hsu, Y. Zhang, W. Wang, T. Kvamsdal, S. Hentschel, J. G. Isaksen, Computational Vascular Fluid-Structure Interaction: Methodology and Application to Cerebral Aneurysms, Biomechanics and Modeling in Mechanobiology 9 (2010) 481–498, ISSN 16177959, doi:\bibinfo{doi}{10.1007/s10237-010-0189-7}.

[11] C. J. Lee, Y. Zhang, H. Takao, Y. Murayama, Y. Qian, The Influence of Elastic Upstream Artery Length on Fluid-Structure Interaction Modeling: A Comparative Study Using Patient-Specific Cerebral Aneurysm, Medical Engineering and Physics 35 (9) (2013) 1377–1384, ISSN 13504533, doi:\bibinfo{doi}{10.1016/j.medengphy.2013.03.009}.

[12] P. Causin, J. F. Gerbeau, F. Nobile, Added-Mass Effect in the Design of Partitioned Algorithms for Fluid-Structure Problems, Computational Methods in Applied Mechanical Engineering 194 (42-44) (2005) 4506–4527, ISSN 00457825, doi:\bibinfo{doi}{10.1016/j.cma.2004.12.005}.

[13] C. Förster, W. A. Wall, E. Ramm, Artificial Added Mass Instabilities in Sequential Staggered Coupling of Nonlinear Structures and Incompressible Viscous Flows, Computer Methods in Applied Mechanics and Engineering 196 (7) (2007) 1278–1293, ISSN 00457825, doi:\bibinfo{doi}{10.1016/j.cma.2006.09.002}.

[14] L. M. Kadasi, W. C. Dent, A. M. Malek, Colocalization of Thin-Walled Dome Regions with Low Hemodynamic Wall Shear Stress in Unruptured Cerebral Aneurysms, Journal of Neurosurgery 119 (1) (2013) 172–179, ISSN 0022-3085, doi:\bibinfo{doi}{10.3171/2013.2.jns12968}.

[15] F. Signorelli, C. Pailler-Mattei, B. Gory, P. Larquet, P. Robinson, R. Vargiolu, H. Zahouani, P.-E. Labeyrie, J. Guyotat, I. Pelissou-Guyotat, J. Berthiller, F. Turjman, Biomechanical Characterization of Intracranial Aneurysm Wall: A Multiscale Study, World Neurosurgery 119 (2018) e882–e889, ISSN 18788750, doi:\bibinfo{doi}{10.1016/j.wneu.2018.07.290}.

[16] J. Frösen, J. Cebral, A. M. Robertson, T. Aoki, Flow-Induced, Inflammation-Mediated Arterial Wall Remodeling in the Formation and Progression of Intracranial Aneurysms, Neurosurgical Focus 47 (1) (2019) E21, ISSN 1092-0684, doi:\bibinfo{doi}{10.3171/2019.5.FOCUS19234}.

[17] S. Soldozy, P. Norat, M. Elsarrag, A. Chatrath, J. S. Costello, J. D. Sokolowski, P. Tvrdik, M. Y. S. Kalani, M. S. Park, The Biophysical Role of Hemodynamics in the Pathogenesis of Cerebral Aneurysm Formation and Rupture, Neurosurgical Focus 47 (1) (2019) 1–9, doi:\bibinfo{doi}{10.3171/2019.4.focus19232}.

[18] H. Meng, V. M. Tutino, J. Xiang, A. Siddiqui, High WSS or Low WSS? Complex Interactions of Hemodynamics with Intracranial Aneurysm Initiation, Growth, and Rupture: Toward a Unifying Hypothesis, American Journal of Neuroradiology 35 (7) (2014) 1254–1262, ISSN 1936959X, doi:\bibinfo{doi}{10.3174/ajnr.A3558}.

[19] J. D. Humphrey, P. B. Canham, Structure, Mechanical Properties, and Mechanics of Intracranial Saccular Aneurysms, Journal of Elasticity 61 (2000) 49–81.

[20] D. V. Parshin, A. I. Lipovka, A. S. Yunoshev, K. S. Ovsyannikov, A. V. Dubovoy, A. P. Chupakhin, On the Optimal Choice of a Hyperelastic Model of Ruptured and Unruptured Cerebral Aneurysm, Scientific Reports 9 (1) (2019) 15865, ISSN 2045-2322, doi:\bibinfo{doi}{10.1038/s41598-019-52229-y}.

[21] G. A. Holzapfel, R. W. Ogden, B. Y. G. E. A. H. Olzapfel, Constitutive Modelling of Arteries, Proceedings of the Royal Society A: Mathematical, Physical and Engineering Sciences 466 (2118) (2010) 1551–1597, ISSN 1364-5021, doi:\bibinfo{doi}{10.1098/rspa.2010.0058}.

[22] V. Costalat, M. Sanchez, D. Ambard, L. Thines, N. Lonjon, F. Nicoud, H. Brunel, J. P. Lejeune, H. Dufour, P. Bouillot, J. P. Lhaldky, K. Kouri, F. Segnarbieux, C. A. Maurage, K. Lobotesis, M. C. Villa-Uriol, C. Zhang, A. F. Frangi, G. Mercier, A. Bonafé, L. Sarry, F. Jourdan, Biomechanical Wall Properties of Human Intracranial Aneurysms Resected Following Surgical Clipping

(IRRAs Project), Journal of Biomechanics 44 (15) (2011) 2685–2691, doi:\bibinfo{doi}{10.1016/j.jbiomech.2011.07.026}.

[23] H. Brunel, D. Ambard, H. Dufour, P. Roche, V. Costalat, F. Jourdan, Rupture Limit Evaluation of Human Cerebral Aneurysms Wall: Experimental Study, Journal of Biomechanics 77 (2018) 76–82, ISSN 00219290, doi:\bibinfo{doi}{10.1016/j.jbiomech.2018.06.016}.

[24] A. M. Robertson, X. Duan, K. M. Aziz, M. R. Hill, S. C. Watkins, J. R. Cebral, Diversity in the Strength and Structure of Unruptured Cerebral Aneurysms, Annals of Biomedical Engineering 43 (7) (2015) 1502–1515, doi:\bibinfo{doi}{10.1007/s10439-015-1252-4}.

[25] R. Kleinloog, E. Korkmaz, J. J. M. Zwanenburg, H. J. Kuijf, F. Visser, R. Blankena, J. A. Post, Y. M. Ruigrok, P. R. Luijten, L. Regli, G. J. E. Rinkel, B. H. Verweij, Visualization of the Aneurysm Wall: A 7.0-Tesla Magnetic Resonance Imaging Study, Neurosurgery 75 (December) (2014) 614–622, doi:\bibinfo{doi}{10.1227/NEU.0000000000000559}.

[26] J. R. Cebral, F. Detmer, B. J. Chung, J. Choque-Velasquez, B. Rezai, H. Lehto, R. Tulamo, J. Hernesniemi, M. Niemela, A. Yu, R. Williamson, K. Aziz, S. Sakur, S. Amin-Hanjani, F. Charbel, Y. Tobe, A. Robertson, J. Frösen, Local Hemodynamic Conditions Associated with Focal Changes in the Intracranial Aneurysm Wall, American Journal of Neuroradiology 40 (3) (2019) 510–516, ISSN 1936959X, doi:\bibinfo{doi}{10.3174/ajnr.A5970}.

[27] R. Torii, M. Oshima, T. Kobayashi, K. Takagi, T. E. Tezduyar, Influence of Wall Elasticity in Patient-Specific Hemodynamic Simulations, Computers and Fluids 36 (2007) 160–168, ISSN 00457930, doi:\bibinfo{doi}{10.1016/j.compfluid.2005.07.014}.

[28] R. Torii, M. Oshima, T. Kobayashi, K. Takagi, T. E. Tezduyar, Fluid-Structure Interaction Modeling of a Patient-Specific Cerebral Aneurysm: Influence of Structural Modeling, Computational Mechanics 43 (2008) 151–159, ISSN 01787675, doi:\bibinfo{doi}{10.1007/s00466-008-0325-8}.

[29] C. J. Lee, Y. Zhang, H. Takao, Y. Murayama, Y. Qian, A Fluid-Structure Interaction Study Using Patient-Specific Ruptured and Unruptured Aneurysm: The Effect of Aneurysm Morphology, Hypertension and Elasticity, Journal of Biomechanics 46 (14) (2013) 2402–2410, ISSN 00219290, doi:\bibinfo{doi}{10.1016/j.jbiomech.2013.07.016}.

[30] A. Valencia, F. Muñoz, S. Arayaa, R. Rivera, E. Bravo, Comparison between Computational Fluid Dynamics, Fluid-Structure Interaction and Computational Structural Dynamics Predictions of Flow-Induced Wall Mechanics in an Anatomically Realistic Cerebral Aneurysm Model, International Journal of Computational Fluid Dynamics 23 (9) (2009) 649–666, ISSN 10618562, doi:\bibinfo{doi}{10.1080/10618560903476386}.

[31] M. Sanchez, D. Ambard, V. Costalat, S. Mendez, F. Jourdan, F. Nicoud, Biomechanical Assessment of the Individual Risk of Rupture of Cerebral Aneurysms: A Proof of Concept, Annals of Biomedical Engineering 41 (1) (2013) 28–40, ISSN 00906964, doi:\bibinfo{doi}{10.1007/s10439-012-0632-2}.

[32] S. Voß, S. Glaßer, T. Hoffmann, O. Beuing, S. Weigand, K. Jachau, B. Preim, D. Thévenin, G. Janiga, P. Berg, Fluid-Structure Simulations of a Ruptured Intracranial Aneurysm: Constant versus Patient-Specific Wall Thickness, Computational and Mathematical Methods in Medicine 2016, doi:\bibinfo{doi}{10.1155/2016/9854539}.

[33] R. Torii, M. Oshima, T. Kobayashi, K. Takagi, T. E. Tezduyar, Fluid-Structure Interaction Modeling of Aneurysmal Conditions with High and Normal Blood Pressures, Computational Mechanics 38 (2006) 482–490, ISSN 01787675, doi:\bibinfo{doi}{10.1007/s00466-006-0065-6}.

[34] K.-C. Cho, H. Yang, J.-J. Kim, J. H. Oh, Y. B. Kim, Prediction of Rupture Risk in Cerebral Aneurysms by Comparing Clinical Cases with Fluid–Structure Interaction Analyses, Scientific Reports 10 (1) (2020) 18237, ISSN 2045-2322, doi:\bibinfo{doi}{10.1038/s41598-020-75362-5}.

[35] Y. Bazilevs, M. C. Hsu, Y. Zhang, W. Wang, X. Liang, T. Kvamsdal, R. Brekken, J. G. Isaksen, A Fully-Coupled Fluid-Structure Interaction Simulation of Cerebral Aneurysms, Computational Mechanics 46 (2010) 3–16, ISSN 01787675, doi:\bibinfo{doi}{10.1007/s00466-009-0421-4}.

[36] M. Sanchez, O. Ecker, D. Ambard, F. Jourdan, F. Nicoud, S. Mendez, J. P. Lejeune, L. Thines, H. Dufour, H. Brunel, P. Machi, K. Lobotesis, A. Bonafe, V. Costalat, Intracranial Aneurysmal Pulsatility as a New Individual Criterion for Rupture Risk Evaluation: Biomechanical and Numeric Approach (IRRAs Project), American Journal of Neuroradiology 35 (2014) 1765–1771, doi:\bibinfo{doi}{10.3174/ajnr.A3949}.

[37] H. Demiray, A Note on the Elasticity of Soft Biological Tissues, Journal of Biomechanics 5 (1972) 309–311, doi:\bibinfo{doi}{10.1016/0021-9290(72)90047-4}.

[38] M. Ramachandran, A. Laakso, R. E. Harbaugh, M. L. Raghavan, On the Role of Modeling Choices in Estimation of Cerebral Aneurysm Wall Tension, Journal of Biomechanics 45 (16) (2012) 2914–2919, ISSN 00219290, doi:\bibinfo{doi}{10.1016/j.jbiomech.2012.07.029}.

[39] T. Passerini, M. Piccinelli, A. Veneziani and L. Antiga, aneurisk, `http://ecm2.mathcs.emory.edu/aneuriskweb/index`, 2021.

[40] VMTK, VMTK Website, `http://www.vmtk.org/`, [Accessed 19-June-2017], 2017.

[41] M. Piccinelli, A. Veneziani, D. A. Steinman, A. Remuzzi, L. Antiga, A Framework for Geometric Analysis of Vascular Structures: Application to Cerebral Aneurysms, IEEE Transactions on Medical Imaging 28 (8) (2009) 1141–1155, doi:\bibinfo{doi}{10.1109/TMI.2009.2021652}.

[42] L. Antiga, B. Ene-Iordache, L. Caverni, G. P. Cornalba, A. Remuzzi, Geometric Reconstruction for Computational Mesh Generation of Arterial Bifurcations from CT Angiography, Computerized Medical Imaging and Graphics 26 (2002) 227–235.

[43] L. Antiga, M. Piccinelli, L. Botti, B. Ene-Iordache, A. Remuzzi, D. A. Steinman, An Image-Based Modeling Framework for Patient-Specific Computational Hemodynamics, Medical and Biological Engineering and Computing 46 (2008) 1097–1112, doi:\bibinfo{doi}{10.1007/s11517-008-0420-1}.

[44] V. Kanyanta, Towards Early Diagnosis of Atherosclerosis: Accurate Prediction of Wall Shear Stress, Ph.D. thesis, 2009.

[45] V. Kanyanta, A. Ivankovic, A. Karac, Validation of a Fluid-Structure Interaction Numerical Model for Predicting Flow Transients in Arteries, Journal of Biomechanics 42 (11) (2009) 1705–1712, ISSN 00219290, doi:\bibinfo{doi}{10.1016/j.jbiomech.2009.04.023}.

[46] E. Tandis, A. Ashrafizadeh, A Numerical Study on the Fluid Compressibility Effects in Strongly Coupled Fluid–Solid Interaction Problems, Engineering with Computers ISSN 14355663, doi:\bibinfo{doi}{10.1007/s00366-019-00880-4}.

[47] M. Mooney, A Theory of Large Elastic Deformation, Journal of Applied Physics 11 (153), doi:\bibinfo{doi}{10.1063/1.1713863}.

[48] G. A. Holzapfel, T. C. Gasser, R. W. Ogden, A New Constitutive Framework for Arterial Wall Mechanics and a Comparative Study of Material Models, Journal of Elasticity 61 (1-3) (2000) 1–48, ISSN 03743535, doi:\bibinfo{doi}{10.1023/A:1010835316564}.

[49] G. A. Holzapfel, Nonlinear Solid Mechanics, John Wiley & Sons, Inc., Chichester, 2000.

[50] Y. Hoi, B. A. Wasserman, Y. J. Xie, S. S. Najjar, L. Ferruci, E. G. Lakatta, G. Gerstenblith, D. A. Steinman, Characterization of Volumetric Flow Rate Waveforms at the Carotid Bifurcations of Older Adults, Physiological Measurement 31 (3) (2010) 291–302, ISSN 09673334, doi:\bibinfo{doi}{10.1088/0967-3334/31/3/002}.

[51] L. Zarrinkoob, K. Ambarki, A. Wåhlin, R. Birgander, A. Eklund, J. Malm, Blood Flow Distribution in Cerebral Arteries, Journal

of Cerebral Blood Flow and Metabolism 35 (2015) 648–654, ISSN 15597016, doi:\bibinfo{doi}{10.1038/jcbfm.2014.241}.

[52] X. C. Chnafa, X. O. Brina, V. M. Pereira, X. D. A. Steinman, Better Than Nothing: A Rational Approach for Minimizing the Impact of Outflow Strategy on Cerebrovascular Simulations, American Journal of Neuroradiology 39 (2018) 337–343, doi:\bibinfo{doi}{10.3174/ajnr.A5484}.

[53] A. Valencia, P. Burdiles, M. Ignat, J. Mura, E. Bravo, R. Rivera, J. Sordo, Fluid Structural Analysis of Human Cerebral Aneurysm Using Their Own Wall Mechanical Properties, Computational and Mathematical Methods in Medicine 2013 (2013) 1–18, ISSN 1748670X, doi:\bibinfo{doi}{10.1155/2013/293128}.

[54] Y.-C. Fung, Biomechanics - Mechanical Properties of Living Tissues, Springer New York, New York, NY, ISBN 978-1-4419-3104-7 978-1-4757-2257-4, doi:\bibinfo{doi}{10.1007/978-1-4757-2257-4}, 1993.

[55] D. Nakagawa, M. Shojima, M. Yoshino, T. Kin, H. Imai, S. Nomura, T. Saito1, H. Nakatomi, H. Oyama1, N. Saito, Wall-to-lumen Ratio of Intracranial Arteries Measured by Indocyanine Green Angiography, Asian Journal of Neurosurgery 11 (2016) 361–364, doi:\bibinfo{doi}{10.4103/1793-5482.175637}.

[56] R. Torii, M. Oshima, T. Kobayashi, K. Takagi, T. E. Tezduyar, Influence of Wall Thickness on Fluid–Structure Interaction Computations of Cerebral Aneurysms, International Journal for Numerical Methods in Biomedical Engineering 26 (2010) 336–347, ISSN 20407939, doi:\bibinfo{doi}{10.1002/cnm}.

[57] K. Furukawa, F. Ishida, M. Tsuji, Y. Miura, T. Kishimoto, M. Shiba, H. Tanemura, Y. Umeda, T. Sano, R. Yasuda, S. Shimosaka, H. Suzuki, Hemodynamic Characteristics of Hyperplastic Remodeling Lesions in Cerebral Aneurysms, PLOS ONE 13 (2018) 1–11, ISSN 1932-6203, doi:\bibinfo{doi}{10.1371/journal.pone.0191287}.

[58] I. L. Oliveira, G. B. Santos, J. Militzer, C. E. Baccin, R. T. Tatit, J. L. Gasche, A Longitudinal Study of a Lateral Intracranial Aneurysm: Identifying the Hemodynamic Parameters behind Its Inception and Growth Using Computational Fluid Dynamics, Journal of the Brazilian Society of Mechanical Sciences and Engineering 43 (2021) 138, doi:\bibinfo{doi}{10.1007/s40430-021-02836-6}.

[59] P. Cardiff, A. Karač, P. De Jaeger, H. Jasak, J. Nagy, A. Ivanković, Ž. Tuković, An Open-Source Finite Volume Toolbox for Solid Mechanics and Fluid-Solid Interaction Simulations, Tech. Rep., 2018.

[60] foam-extend Project, foam-extend Website, `https://sourceforge.net/projects/foam-extend/`, [Accessed 19-June-2017], 2017.

[61] H. G. Weller, G. Tabor, H. Jasak, C. Fureby, A Tensorial Approach to Computational Continuum Mechanics Using Object-Oriented Techniques, Computers in Physics 12 (1998) 620–631.

[62] R. I. Issa, Solution of the Implicitly Discretised Fluid Flow Equations by Operator-Splitting, Journal of Computational Physics 62 (1) (1986) 40–65, ISSN 10902716, doi:\bibinfo{doi}{10.1016/0021-9991(86)90099-9}.

[63] H. Jasak, Error Analysis and Estimation for the Finite Volume Method with Applications to Fluid Flows, Ph.D. thesis, Imperial College, 1996.

[64] M. A. Wheel, A Mixed Finite Volume Formulation for Determining the Small Strain Deformation of Incompressible Materials, International Journal for Numerical Methods in Engineering 44 (1999) 1843–1861.

[65] NumPy, NumPy Website, `https://numpy.org/`, [Accessed 05-May-2022], 2017.

[66] SciPy, SciPy Website, `https://www.scipy.org`, [Accessed 05-May-2022], 2017.

[67] M. A. Castro, Understanding the Role of Hemodynamics in the Initiation, Progression, Rupture, and Treatment Outcome of Cerebral Aneurysm from Medical Image-Based Computational Studies, ISRN Radiology (2013) 1–17doi:\bibinfo{doi}{10.

5402/2013/602707}.

[68] J. R. Cebral, M. Vazquez, D. M. Sforza, G. Houzeaux, S. Tateshima, E. Scrivano, C. Bleise, P. Lylyk, C. M. Putman, Analysis of Hemodynamics and Wall Mechanics at Sites of Cerebral Aneurysm Rupture, Journal of NeuroInterventional Surgery 7 (7), ISSN 1759-8478, doi:\bibinfo{doi}{10.1136/neurintsurg-2014-011247}.

[69] G. A. Holzapfel, R. W. Ogden (Eds.), Biomechanics of Soft Tissue in Cardiovascular Systems, Springer Vienna, Vienna, ISBN 978-3-211-00455-5 978-3-7091-2736-0, doi:\bibinfo{doi}{10.1007/978-3-7091-2736-0}, 2003.

**Supplementary Material**

**Influence of Local Thickness and Material Constants**

Two parametric studies were carried out by changing the scale factors applied to build the abnormal-wall model by scaling the thickness and material constants of type-I and type-II patches. A simpler modeling of the flow was applied, though, by using a steady-state blood flow model at peak-systole conditions as the driven force of the arterial and IA wall motion and numerically solving it with the 1WFSI strategy with the same BCs presented in main study. Only the Yeoh hyperelastic law was used — it is reasonable to assume that the same behavior would be found for the MR and Fung laws —, with $\nu^{\mathrm{s}} = 0.48$. The study was carried out in two stages: first, by varying $e_{ia}$, locally, and, in the sequence, changing the fields of the the material constants, $c_1$ and $c_2$.

In the first stage, uniform elasticities over the aneurysm, $c_1$ and $c_2$, were assumed to isolate the effect of the varying $e_{ia}$ on each patch type, calculated as follows:

1. on type-I patches, $e_{ia}$ was first kept unchanged and then decreased by 5, 10, 20, and 30 %, while keeping the type-II patches 20 % thicker;
2. on type-II patches, $e_{ia}$ was first kept unchanged and then increased by 5, 10, 20, and 30 %, while keeping the type-I patches 5 % thinner.

The computational meshes were created similarly as in the main study, but, in this case, for each new thickness field, a new mesh was generated, whereas a single fluid computational mesh was used.

In the second stage, uniform $e_{ia}$ was assumed over $S^{\mathrm{l}}_{ia}$ — thus, a single mesh was used — to isolate the effect of varying the material constants, $c_1$ and $c_2$, which were both, first, kept uniform and, then, decreased by 10, 20, and 30 %, on type-I and type-II patches at the same time.

Note that the parametric intervals employed ($[5\,\%, 30\,\%]$) included the actual values selected for the abnormal wall morphology model. The surface-averages of $\sigma_1$ and $\lambda_1$ were computed over $S^{\mathrm{l}}_{ia}$ at the deformed configuration. The results are shown in Fig. S1.

The plots show how $\langle \sigma_1 \rangle_{S^{\mathrm{l}}_{ia}}$ and $\langle \lambda_1 \rangle_{S^{\mathrm{l}}_{ia}}$ changed with both local changes in $e_{ia}$ and $c_{ij}$. The absolute difference between the extremes of the parametric intervals was computed for each IA case, and its average annotated above each plot.

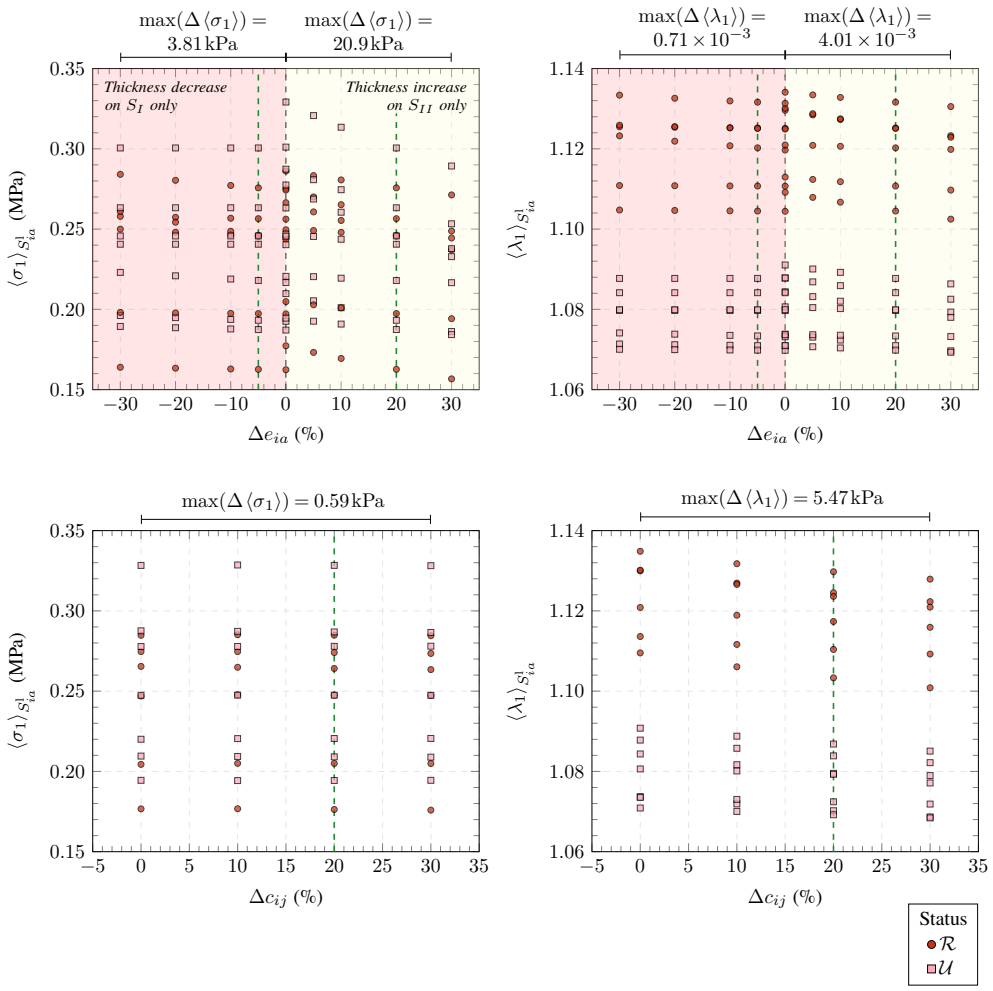


Figure S1: Surface-averaged $\sigma_1$ (left column) and $\lambda_1$ (right column) over $S^{\mathrm{l}}_{ia}$, grouped by rupture status, versus the percentual variation of $e_{ia}$ (first row) and material constants, $c_{10}$ and $c_{20}$, (second row) applied separately on type-I and type-II patches. Above each plots is annotated the mean maximum absolute difference among all IAs.